




# Photocatalytic disinfection efficiency of 2D structure graphitic carbon nitride-based nanocomposites: a review

Pramila Murugesan<sup>1</sup>, J. A. Moses<sup>1</sup>, and C. Anandharamakrishnan<sup>1,\*</sup> 

<sup>1</sup> Computational Modeling and Nanoscale Processing Unit, Indian Institute of Food Processing Technology (IIFPT), Ministry of Food Processing Industries, Government of India, Thanjavur, Tamil Nadu, India

Received: 9 February 2019

Accepted: 20 May 2019

Published online:

28 May 2019

© Springer Science+Business Media, LLC, part of Springer Nature 2019

## ABSTRACT

Nanostructured carbon-based photocatalysts have gained attention in photocatalytic disinfection of microbial species. With distinctive features of possessing appropriate electronic band gap structure and high chemical and thermal stability, metal-free polymeric 2D stacked structure graphitic carbon nitride ( $g\text{-C}_3\text{N}_4$ ) is an important photocatalytic material for environmental and energy applications. Besides, it has the potential for inactivation of harmful pathogens. Disinfection of microbial species is mainly ascribed to the formation of reactive oxidative species. Further, surface modification of  $g\text{-C}_3\text{N}_4$  can remarkably improve photocatalytic disinfection efficiency. In this review, we have discussed the recent advances in photocatalytic disinfection using  $g\text{-C}_3\text{N}_4$ -based nanocomposites. An overview of metal-free nanostructure  $g\text{-C}_3\text{N}_4$ , metal (anions) and nonmetal (cations)-doped  $g\text{-C}_3\text{N}_4$  and  $g\text{-C}_3\text{N}_4$  hybridized with low band gap semiconductor is also presented. Moreover, we have emphasized on the photocatalytic disinfection mechanism associated with  $g\text{-C}_3\text{N}_4$ -modified composites. Nitrogen-rich  $g\text{-C}_3\text{N}_4$  polymeric material can serve as an alternative to metal oxide ( $\text{TiO}_2$  and  $\text{ZnO}$ ) photocatalysts for photocatalytic disinfection technology. Other applications such as  $\text{CO}_2$  photoreduction,  $\text{H}_2$  generation, organic pollutant degradation, and sensing using  $g\text{-C}_3\text{N}_4$ -based nanocomposites are also summarized.

## Introduction

Elimination of microbial load has been a significant concern owing to threat associated with several infections through food, water, and a range of other mode of infection. In particular, solid surfaces act as a

reservoir for surviving gram negative ( $G^-$ ) [*Escherichia coli* (*E. coli*), *Klebsiella pneumoniae* (*K. pneumoniae*)], gram positive ( $G^+$ ) [*Enterococcus faecalis* (*E. faecalis*), *Staphylococcus aureus* (*S. aureus*)] and fungal pathogen (*Candida albicans*) [1]. Hence, numerous efforts have been taken for remediating microbial contamination

Address correspondence to E-mail: anandharamakrishnan@iifpt.edu.in

including conventional chemical disinfectants (chlorine, chlorine dioxide, ozone, and alcohol, formaldehyde, or hydrogen peroxide) and ultraviolet irradiation (UV-C, UV-B and UV-A) [2–4]. However, such methods have drawbacks of time-limited antimicrobial activity, generation of toxic carcinogenic by-products such as trihalomethanes to the environment, and high operational costs [5]. Hence, it is vital to develop simple, low cost, and effective antimicrobial approaches for reducing harmful microbial load in the environment.

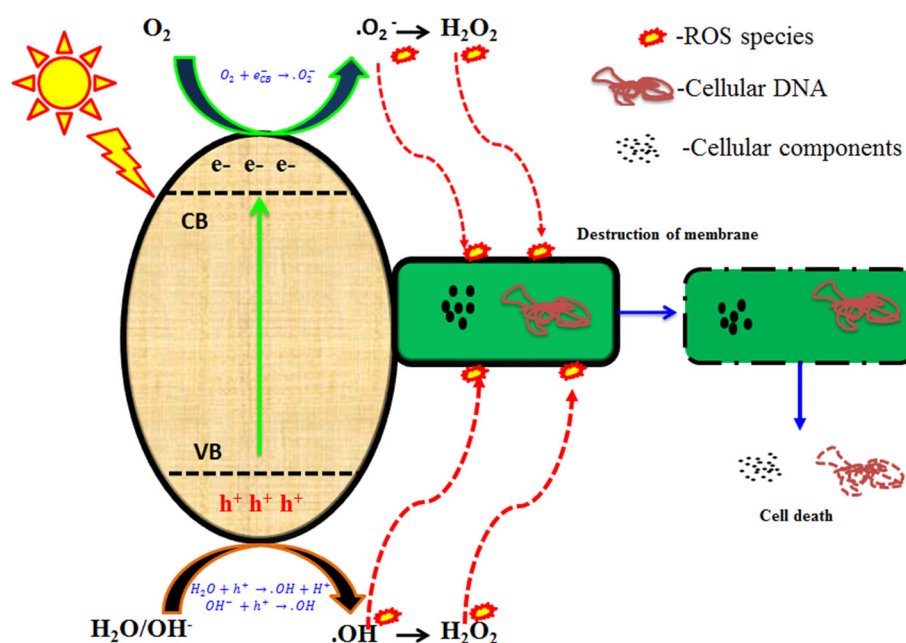
In recent years, nanocomposite-based photocatalytic disinfection processes have gained interest on a commercial scale as an approach to reduce microbial contamination [6, 7]. Photocatalytic disinfection relies on the principle of photoexcitation of a semiconductor material upon absorption of light, the wavelength of light being higher than the band gap energy level of semiconductor material (Fig. 1). In this process of exposure to light, electrons in the valence band (VB) get excited and move to the conduction band (CB) of the semiconductor material. This leaves a photogenerated hole in the VB. Finally, photogenerated holes and electrons pairs are involved in redox reactions. The production of reactive oxygen species (ROS) during photocatalysis can induce leakage of minerals, genetic material, and protein and thus result in cell death and reduction in microbial load.

In this aspect, metal oxides like titanium dioxide ( $\text{TiO}_2$ ), zinc oxide ( $\text{ZnO}$ ), magnesium oxide ( $\text{MgO}$ ),

and tin oxide ( $\text{WO}_3$ ), and nonmetal oxides such as graphitic carbon nitride ( $\text{g-C}_3\text{N}_4$ ), multiwall carbon nanotube (MWCNT), and graphene oxide (GO) semiconductor photocatalysts have been developed and employed for inactivation of microbial species [8–12]. However, intermediate or narrow bandgap semiconductors that have the capability to reduce molecular oxygen ( $\text{O}_2$ ) to cytotoxic ROS show a promising scope for decreasing microbial load in the environment. Of late, Wang et al. [13] reported that metal-free treated rape pollen (TRP) displays remarkable inactivation efficiency toward the different waterborne bacterial species including *E. Coli* K-12, *Pseudomonas aeruginosa* (*P. aeruginosa*), *S. aureus*, and *Bacillus pumilus* (*B. pumilus*). Owing to higher specific surface area, more number of surface-active sites, improved chemical stability, and conductivity, 2D nanomaterial display outstanding antibacterial activity as compare with 1D nanomaterials.

Till date, 2D-structured metal-free polymeric  $\text{g-C}_3\text{N}_4$  semiconductor materials have been extensively used for antimicrobial applications [14, 15]. At first, Wang and co-workers [16] synthesized  $\text{g-C}_3\text{N}_4$  for a hydrogen ( $\text{H}_2$ ) evaluation reaction. There has been a significant rise in scientific interest on the development of  $\text{g-C}_3\text{N}_4$ -based materials for energy and environmental applications. Benefiting from its distinctive properties (i.e., appropriate band gap (2.7 eV), high chemical, mechanical, and thermal stability),  $\text{g-C}_3\text{N}_4$  is popularly used in waste water

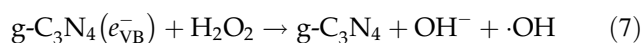
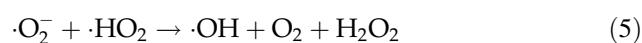
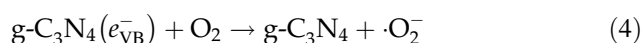
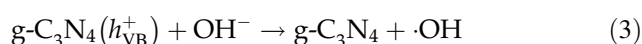
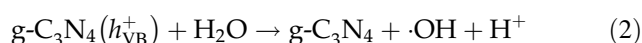
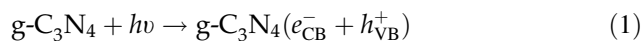
**Figure 1** Schematic illustration of semiconductor-based photocatalytic disinfection mechanism of microbial species.



treatment [17], water splitting [18], NO<sub>x</sub> fixation [19], CO<sub>2</sub> conversion [20], and sensing applications [21]. Nevertheless, because of some known drawbacks (i.e., high recombination rate of photogenerated charge carriers and inadequate utilization of visible light) of g-C<sub>3</sub>N<sub>4</sub>, several surface-modified and improved techniques have been devoted for enhancing its photocatalytic efficiency. This review critically reviews the emerging trends in disinfection using g-C<sub>3</sub>N<sub>4</sub>-based photocatalysts. A summary of theoretical advances and basic principle for microbial inactivation using g-C<sub>3</sub>N<sub>4</sub> are also discussed.

### Basic principle of photocatalytic disinfection mechanism on g-C<sub>3</sub>N<sub>4</sub>

Photocatalytic disinfection mechanism of g-C<sub>3</sub>N<sub>4</sub> is explained by the formation of photogenerated charge carriers (electron and hole pair) when exposed to light. Overall electron transfer and formation of ROS species on g-C<sub>3</sub>N<sub>4</sub> surface is explained using Eqs. (1–7) [22, 23]. Photogenerated electrons get excited from VB to CB; then, these charge carriers transfer to g-C<sub>3</sub>N<sub>4</sub> surface and initiate a series of reactions and generate highly active ROS species. Generally, hydroxyl ( $\cdot\text{OH}$ ) radical, hydrogen peroxide (H<sub>2</sub>O<sub>2</sub>), and superoxide ( $\cdot\text{O}_2^-$ ) are key species responsible for photocatalytic disinfection [24–26]. It is known that holes ( $h^+$ ) in the VB can decompose (oxidize) water into  $\cdot\text{OH}$  radicals, thereby contributing to the inactivation of microbial species, especially bacteria. Moreover, other ROS species (H<sub>2</sub>O<sub>2</sub> and  $\cdot\text{O}_2^-$ ) are mainly formed from reduction of O<sub>2</sub> (O<sub>2</sub> →  $\cdot\text{O}_2^-$  ↔  $\cdot\text{HO}_2$  → H<sub>2</sub>O<sub>2</sub> ↔  $\cdot\text{OH}$ ), as they effectively react with cellular compounds, membrane leakage of microbial cell walls, and ultimately cause cell death [27, 28].



### Structure of g-C<sub>3</sub>N<sub>4</sub>

g-C<sub>3</sub>N<sub>4</sub> is a class of  $\pi$ -conjugative polymeric n-type semiconductor and consists primarily of carbon and nitrogen (Fig. 2) [18, 29]. Polymeric g-C<sub>3</sub>N<sub>4</sub> was first synthesized by Berzelius and named by Liebig in 1834 [30]. Then, its structure was described by Franklin in 1922 [31]. Importantly, among all allotropes of carbon nitrides at ambient atmosphere, g-C<sub>3</sub>N<sub>4</sub> is not only the most stable, but it also has distinctive surface properties (basic surface functionalities, electron-rich properties and H-bonding motifs) that are essential for many photocatalytic applications [32, 33]. Also, the C–N layers in the g-C<sub>3</sub>N<sub>4</sub> have a laminar structure with weak van der Waals interactions, which is similar to the structure of graphite [34]. Mainly, it contains of a long pair of nitrogen-based triazine/tri-s-triazine tectonic units and can be easily prepared from low-cost nitrogen-rich feedstocks such as melamine, melamine hydrochloride, urea, thiourea, and dicyandiamide [16, 20, 35–43].

Solvothermal [44], molecular self-assembly [45], microwave irradiation [46], and thermal polycondensation methods [47] are common synthesis approaches to prepare g-C<sub>3</sub>N<sub>4</sub>-based photocatalysts. Chemical synthesis of g-C<sub>3</sub>N<sub>4</sub> has the benefits of formation of uniform and fine particle, limited energy utilization, while the process is economically feasible. Powder form of g-C<sub>3</sub>N<sub>4</sub> was synthesized by heating the dicyandiamide with barbituric acid (C<sub>4</sub>H<sub>4</sub>N<sub>2</sub>O<sub>3</sub>, BA) mixture at 550 °C in air [30]. Benzene thermal reaction between 1,3,5-trichloromelamine (C<sub>3</sub>N<sub>3</sub>Cl<sub>3</sub>) and sodium amide (NaNH<sub>2</sub>) at 180–220 °C for 8–12 h was adapted for preparation of well crystalline g-C<sub>3</sub>N<sub>4</sub> nanocrystals [48]. Tubular luminescent polymeric networks of g-C<sub>3</sub>N<sub>4</sub> has been synthesized using solvothermal route, involving the reaction of 1,3,5-trichlorotriazine (C<sub>3</sub>N<sub>3</sub>Cl<sub>3</sub>) with ammonium chloride (NH<sub>4</sub>Cl) in the presence of iron powder at 300 °C [49]. However, it requires several hours for formation of particle and crystallization. Microwave synthesis route has also been explored for synthesizing submicrosphere g-C<sub>3</sub>N<sub>4</sub> using cyanuric chloride and sodium azide powder as a precursor for a 30-min time period [50]. Recently, microwave-assisted solvothermal process has been employed for the development of visible light-active tri-s-triazine (C<sub>6</sub>N<sub>7</sub>) unit-based g-C<sub>3</sub>N<sub>4</sub> photocatalysts as shown in Fig. 3 [51]. Nitrogen-rich carbon nitride films were

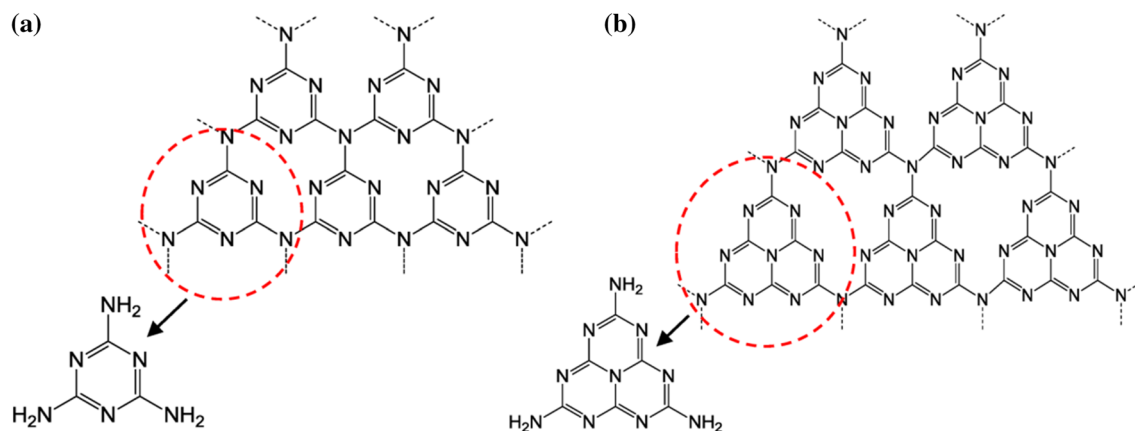


**Figure 2** **a** Triazine and **b** tri-s-triazine (heptazine) structures of  $g\text{-C}_3\text{N}_4$  [157].

prepared by thermal vapor transport under Ar flow onto the Si and  $\text{SiO}_2$  substrates at 250–350 °C [52]. Kang et al. [53] fabricated  $g\text{-C}_3\text{N}_4$  nanosheets from bulk  $g\text{-C}_3\text{N}_4$  using facile bacterial liquid exfoliation method (bioetching method) (Fig. 4). The optical and textural properties of  $g\text{-C}_3\text{N}_4$  may be affected by different preparation conditions and types of precursors used [54, 55]. For instance, urea-derived  $g\text{-C}_3\text{N}_4$  shows a slightly larger energy band gap as compared with  $g\text{-C}_3\text{N}_4$  obtained from thiourea [56]. A summary of physicochemical properties and multi-functional application of  $g\text{-C}_3\text{N}_4$ -based composite is presented in Fig. 5.

### Modification strategy of $g\text{-C}_3\text{N}_4$

Surface modification and band gap configuration of the pristine  $g\text{-C}_3\text{N}_4$  can lead to improvement in its photocatalytic performance. Exfoliation of pristine  $g\text{-C}_3\text{N}_4$  into  $g\text{-C}_3\text{N}_4$  nanosheets showed larger surface area and effective charge transfer. Structure defect engineering is valuable route for improving the photocatalytic activity of  $g\text{-C}_3\text{N}_4$ . Modification of surface property is favorable for strengthening the adsorption of reactants on its surface and controlling recombination rate of charge carriers, and thus accelerating the surface catalytic reactions. Optimization of crystal structure can efficiently change the electronic property and oxidation and reduction ability of photogenerated charge carriers. Designing

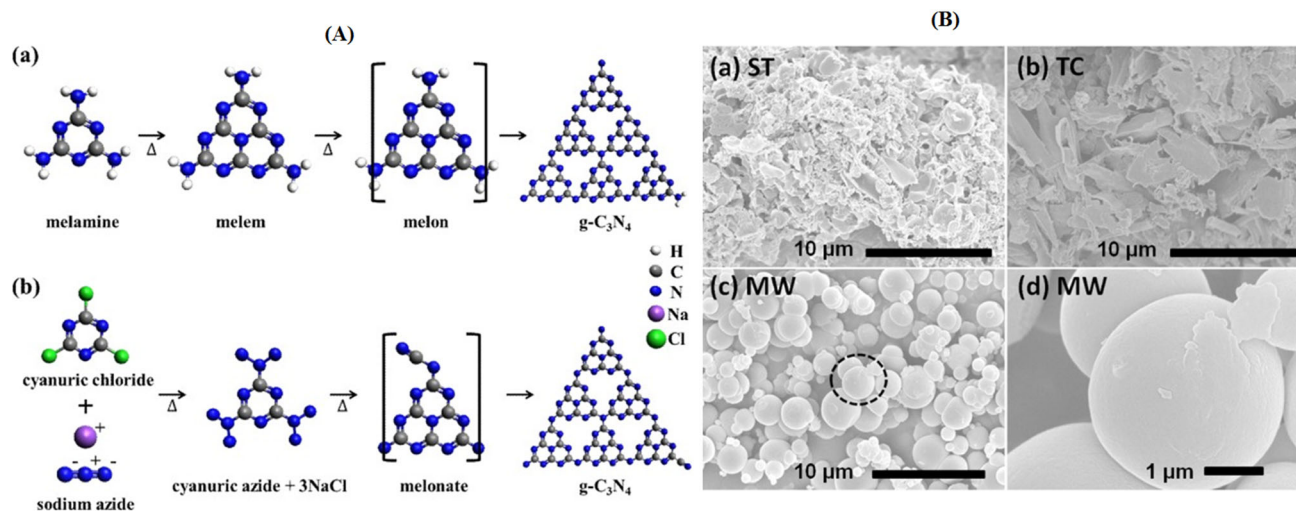


**Figure 3** **A** Formation mechanism of graphitic carbon nitride obtained from (a) thermal condensation (TC) of melamine and (b) traditional and microwave (MW)-assisted solvothermal

methods (ST) using cyanuric chloride and sodium azide as precursors and **B** SEM images of (a) ST, (b) TC, and (c) MW samples; (d) magnification of MW sample [51].



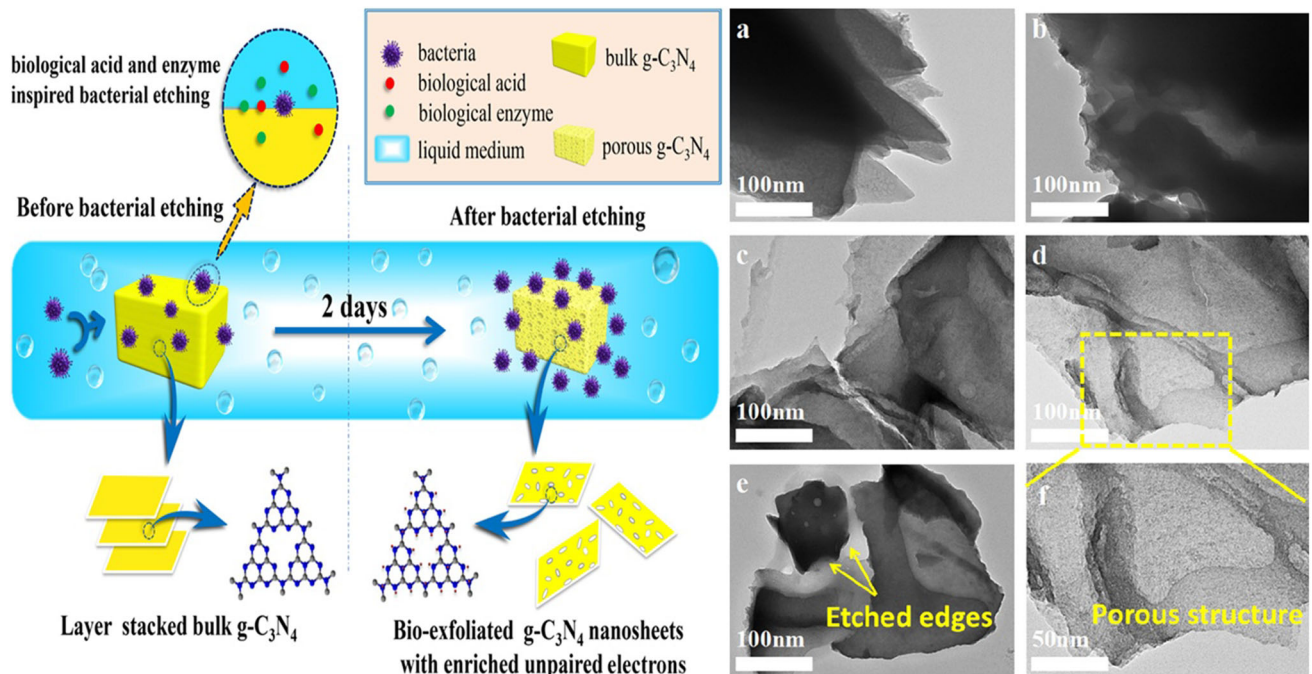
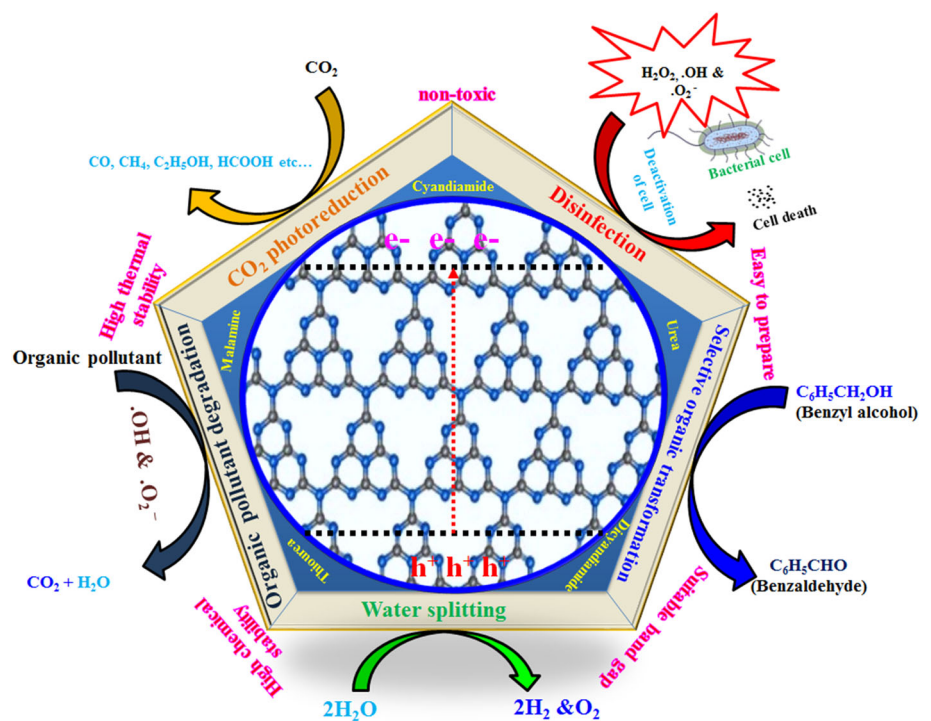


**Figure 4** A Proposed bacterial-inspired synthesis process and mechanism of bacteria-treated (BT)  $g\text{-C}_3\text{N}_4$  samples and (b) TEM images of (a)  $g\text{-C}_3\text{N}_4$ , (b) bacteria untreated  $g\text{-C}_3\text{N}_4$  (c) BT-  $g\text{-C}_3\text{N}_4$ -4 h, (d, f) BT-  $g\text{-C}_3\text{N}_4$  -2d and (e) BT-  $g\text{-C}_3\text{N}_4$  -5d samples [53].

of nanostructures ( $g\text{-C}_3\text{N}_4$  nanotube,  $g\text{-C}_3\text{N}_4$  nanorods, and mesoporous  $g\text{-C}_3\text{N}_4$ ) is an efficient approach for improving the photocatalytic efficiency.  $g\text{-C}_3\text{N}_4$  nanostructured materials provides large pores, high

surface area, improved reactant/product diffusion, and showed multiple light scattering effect. Hybrid structure construction is considered as the most viable method to improve the separation efficiency of

**Figure 5** Schematic representations of physicochemical properties and multi-functional application of  $g\text{-C}_3\text{N}_4$ .



charge carriers, which greatly enhances the photocatalytic performance. With respect to the charge separation mechanism of  $g\text{-C}_3\text{N}_4$ -based hybrid structure, it can be categorized into the following types as follows (Fig. 6).

- Type I heterojunction
- Type II heterojunction
- $p\text{-}n$  heterojunction
- Schottky junction
- Z-scheme heterojunction

Type I heterojunction, semiconductor I (SC1) has higher VB and higher CB position. During photocatalysis, holes in the VB of SC1 get shifted to the VB of semiconductor II (SCII). Meanwhile, photogenerated electrons in SC I migrate toward SCII; thereby, charge carriers are separated. For instance, type I heterojunction morphologies such as  $\text{SnS}_2$  (nanoparticles, nanosheets and 3D flower-like) hybridized  $g\text{-C}_3\text{N}_4$  composites exhibit better photocatalytic activity toward  $\text{H}_2$  generation and also show excellent stability [57]. Notably, charge carriers are

accumulated on  $\text{SnS}_2$  surface, yielding no improvement in charge separation. Type II heterojunction consists of  $g\text{-C}_3\text{N}_4$  and another low or large band gap semiconductor. After the excitation process, photogenerated electrons move from high CB position to low CB position and holes get transferred from the highest VB potential to the lowest VB potential. Finally, the internal field facilitates separation and movement of photogenerated charge carriers.

For example, Kong et al. [58] established that metal-free type II heterojunction of 0D black phosphorus quantum dots (BPQDs) with 2D  $g\text{-C}_3\text{N}_4$  composites exhibited improved stability and vigorous photocatalytic efficiency. Type II heterojunction system is not adequate to conquer the high recombination rates in photogenerated systems. The  $p\text{-}n$  heterojunction photocatalyst obtained by blending  $p$ -type and  $n$ -type semiconductor materials can provide an additional electric field to accelerate charge transfer for improving photocatalytic activity. Before light irradiation, holes in the  $p$ -type semiconductor material are transferred to the  $n$ -type semiconductor,

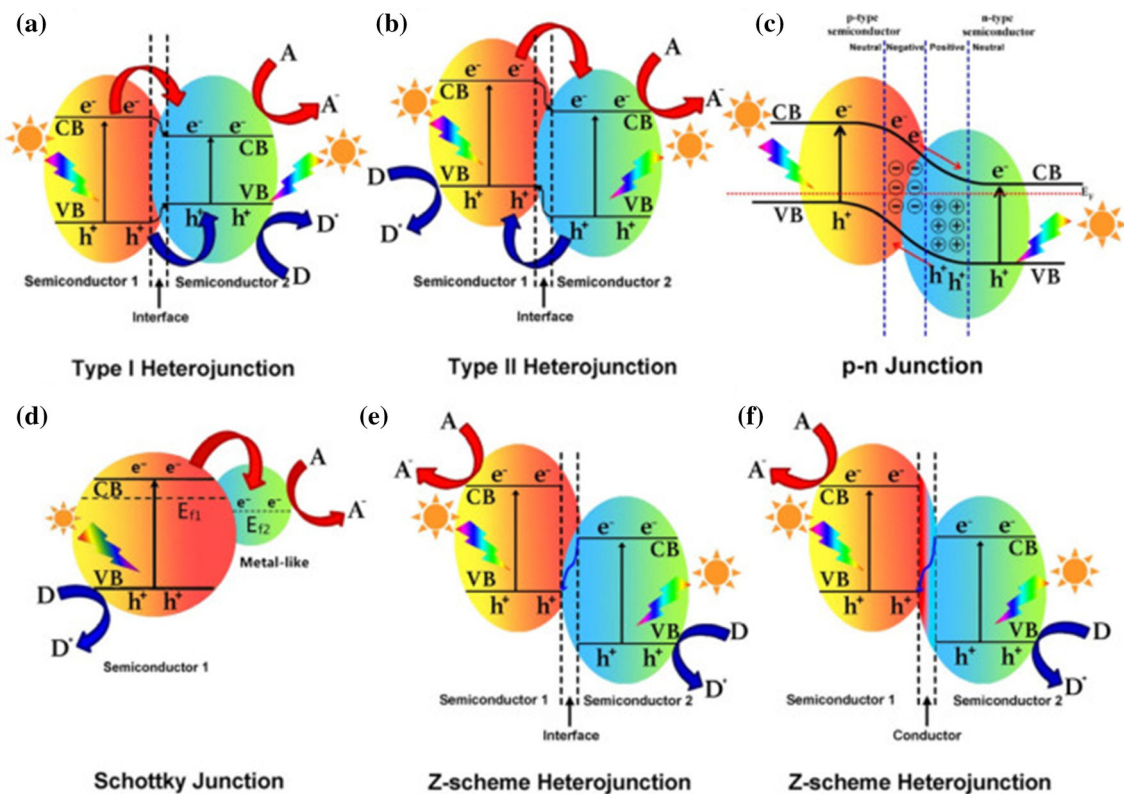


**Figure 6** Different types of  $g\text{-C}_3\text{N}_4$ -based heterojunctions: **a** Type I heterojunction, **b** Type II heterojunction, **c**  $p\text{-}n$  junction, **d** Schottky junction, **e** Z-scheme heterojunction (without an

electron mediator) and **f** indirect Z-scheme (with an electronmediator). Note  $A$ ,  $D$  and  $E_F$  represent electron acceptor, electron donor and fermi level respectively) [14].

leaving photogenerated electrons. The transfer of electron–hole pairs will refrain when the fermi level system attains equilibrium.

$g\text{-C}_3\text{N}_4$  is an  $n$ -type semiconductor material because it has  $\text{NH}/\text{NH}_2$  groups in its structure. Therefore, designing of  $p$ – $n$  heterojunction can normally boost the photocatalytic efficiency of  $g\text{-C}_3\text{N}_4$ .  $\text{Ag}_2\text{O}$  is a attractive  $p$ -type semiconductor material, which has narrow band gap (1.2 eV) with efficient absorbance of UV–Vis–NIR light. A  $p$ – $n$  heteriojunction of  $\text{Ag}_2\text{O}/g\text{-C}_3\text{N}_4$  prepared by simple chemical precipitation method and can posses enhanced photocatalytic activity toward organic pollutants degradation. Enhanced photocatalytic efficiency is attributed to strong high separation efficiency of photogenerated electron–hole pairs, UV–Vis–NIR light absorption, and surface plasmon effect of metal Ag [59].

Schottky effect is evident at metal–semiconductor interface due to difference in fermi levels, and this generates the built-in electric field and drives the charge flow until the system reaches a state of equilibrium. Therefore, fermi energy levels can be aligned and the recombination of charge carriers is controlled to enhance photocatalytic performance. Furthermore, selection of a suitable metallic co-catalyst with superior charge mobility, low overpotential, and large metal–semiconductor interface to enhance the Schottky effect may be advantageous in boosting the photocatalytic behavior of  $\text{H}_2$  generation. Remarkable improvement in photocatalytic  $\text{H}_2$  evolution activity over 2D–2D  $\text{CoP}/g\text{-C}_3\text{N}_4$  composites can be attributed to effective carrier separation introduced by Schottky effect, low overpotential and good electron mobility of  $\text{CoP}$ , and shortened transportation distance of charge transfer in the 2D/2D composite photocatalysts [60]. In another study, Schottky catalyst of metallic  $\text{MoN}$ -coupled  $n$ -type  $g\text{-C}_3\text{N}_4$  displayed boosted efficiency for  $\text{H}_2$  generation and rhodamine blue (Rh B) degradation over bare  $g\text{-C}_3\text{N}_4$  due to improved charge separation and transportation [61].

In a Z-scheme-based heterojunction system, electrons on the lower value CB of SC II directly combine with VB of SC I. Several studies have explored scheme systems with and without electron mediators. Commonly, nanoscale metals such as Ag and Au as electron mediators have been used for constructing Z-scheme systems, owing to good electrical conductivity. Z-scheme heterojunction of binary  $\text{LaMnO}_3/g\text{-C}_3\text{N}_4$

hybrid nanocomposite not only separates the charge carrier but also endows the  $\text{LaMnO}_3/g\text{-C}_3\text{N}_4$  photocatalyst with strong redox ability, thus boosting the degradation efficiency of tetracycline compound. In another case, the formation of Z-scheme  $g\text{-C}_3\text{N}_4/\text{Ag}/\text{Ag}_3\text{PO}_4$  (rhombohedral dodecahedrons morphology) heterojunction via simple in situ deposition method possesses advanced efficiency of charge separation and transfer, as well as stronger redox ability [62].

### Theoretical advances on the $g\text{-C}_3\text{N}_4$ -based nanocomposites

Generally, there exists seven different phases of  $\text{C}_3\text{N}_4$  with different band gap energies (Table 1). The nitride pores' size and various electronic environments of the N atom connect to various energetic stabilities. On the basis of density functional theory (DFT), Kroke et al. [63] demonstrated that tri-*s*-triazine-based structure is energetically favored and is the most stable structure among all allotropes of  $g\text{-C}_3\text{N}_4$ . It is flexible for inducing reactions to alter its surface activity without altering its theoretical structure and composition. It exhibits advantages of strong physicochemical stability and distinctive electronic band structure, owing to high degree of condensation and the presence of heptazine ring structure. Due to the presence of the tri-*s*-triazine ring structure,  $g\text{-C}_3\text{N}_4$  is stable up to 600 °C, in  $\text{N}_2$ ,  $\text{O}_2$ , and air atmospheres [34, 64]. It possesses nitrogen-rich, Lewis and Bronsted basic sites, and shows good potential in  $\text{CO}_2$  fixation and activation. High thermal stability implies that  $g\text{-C}_3\text{N}_4$  can suit for both under oxidative and higher temperatures atmospheres.

**Table 1** Different phases of  $g\text{-C}_3\text{N}_4$  [159, 160]

$g\text{-C}_3\text{N}_4$	Band gap (eV)
Alpha	5.5
Beta	4.85
Cubic	4.3
Pseudocubic	4.13
<i>g</i> - <i>h</i> -triazine	2.97
<i>g</i> - <i>o</i> -triazine	0.93
<i>g</i> - <i>h</i> -heptazine	2.87

Note *g*-*h*-triazine-hexagonal unit cell of  $g\text{-C}_3\text{N}_4$ , *g*-*o*- triazine-orthorhombic unit cell and *g*-*h*-heptazine-three fused *s*-triazine rings connected by nitrogen atoms.



Besides,  $g\text{-C}_3\text{N}_4$  offers good chemical stability in a varied range of solvents such as toluene, diethyl ether, dimethylformamide, water, and alcohols, making it an effective catalyst for both gas and liquid phase reactions [29, 65, 66].

The morphological structure of  $g\text{-C}_3\text{N}_4$  plays a substantial role in photocatalysis. Fine control and unique oriented structure of  $g\text{-C}_3\text{N}_4$  is useful for energy harvesting, conversion, and storage application [67]. Chen et al. [68] explained cleavage of in-plane hydrogen bonds between polymeric melon units by the introduction of  $\text{CO}_3^{2-}$  which promote amorphization of  $g\text{-C}_3\text{N}_4$  and increase visible light absorption ability [69]. Usually, CN has weak van der Waals (vdW) interlayer interactions. Li et al. [70] demonstrated that forming internal van der Waals heterostructures (IVDWHs) within  $g\text{-C}_3\text{N}_4$  can augment interlayer Coulomb interaction and assist charge separation efficiency. Moreover, urea-derived  $g\text{-C}_3\text{N}_4$  possess strong redox ability, effective absorption of contaminants, and efficient charge separation efficiency, due to its large band gap, large surface area, and moderated N-defects [71]. Besides, it has five substitutional sites and two interstitial sites are usually considered as doping sites (Fig. 7). Doping of  $g\text{-C}_3\text{N}_4$  alters its geometric structure and electronic and optical properties. For instance, Cui et al. [72] demonstrated that introduction of O on the surface of  $g\text{-C}_3\text{N}_4$  can extend the absorption of visible light absorption and promote delocalization of HOMO and LUMO. Fabrication of modified  $g\text{-C}_3\text{N}_4$ -based heterojunction nanocomposites with enhanced physicochemical properties for better photocatalytic activity is an emerging concept for precise applications. The better photocatalytic mechanism for  $g\text{-C}_3\text{N}_4/\text{MoS}_2$  hybrid nanocomposites by DFT calculations was reported by Wang et al. [73]. DFT calculations explain that these hybrid nanocomposites possess improved separation of photogenerated carriers.

Adsorption of reactants photocatalysts surface is significant in photocatalysis because it is directly related with several reactions. Adsorption energies of  $\text{H}_2\text{O}$ ,  $\text{CO}_2$ ,  $\text{H}_2$ ,  $\text{N}_2$ ,  $\text{CO}$ , and  $\text{CH}_4$  on  $g\text{-C}_3\text{N}_4$  are reported to be  $-0.513$ ,  $-0.226$ ,  $-0.078$ ,  $-0.117$ ,  $-0.155$  and  $-0.163$  eV, respectively [74]. Interestingly, adsorption energies of products are more positive than those of reactants, implying strong adsorption of reactants onto  $g\text{-C}_3\text{N}_4$  and easy desorption of products from  $g\text{-C}_3\text{N}_4$ , which are

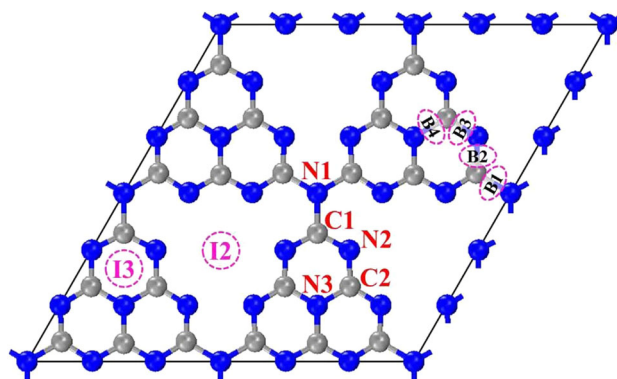


**Figure 7** Eleven adsorption sites in tri-s-triazine-based  $g\text{-C}_3\text{N}_4$  [158].

noticeably beneficial to start the reaction and reappear adsorption sites, respectively.

It is well established that there are two different half reactions involved in photocatalytic water splitting process: hydrogen generation via  $\text{H}^+$  reduction and  $\text{O}_2$  generation via  $\text{H}_2\text{O}$  oxidation. As the standard redox potential for formation of both products ( $\text{O}_2/\text{H}_2\text{O} = 1.23$  V vs. NHE and  $\text{H}_2/\text{H}^+ = 0$  V vs. NHE) lies within the CB and VB potential of  $g\text{-C}_3\text{N}_4$ , it is theoretically evident that  $g\text{-C}_3\text{N}_4$  can catalyze overall water splitting reactions. Wirth et al. [75] studied water splitting reaction over  $g\text{-C}_3\text{N}_4$  using DFT calculation. They reported that the overpotential for  $\text{H}_2\text{O}$  oxidation reaction is more than that of  $\text{H}^+$  reduction process, thus implying that  $\text{O}_2$  generation process demand oxidation co-catalyst, while  $\text{H}_2$  production can be simply attained without a co-catalyst. Nevertheless, its usage for antimicrobial coating applications is not fully explored owing to challenges associated with limited absorption of visible region and higher recombination rate of photogenerated charge carriers [76, 77].

### **$g\text{-C}_3\text{N}_4$ -based photocatalysts for disinfection applications**

Different strategies have been adopted to resolve problems associated with pristine  $g\text{-C}_3\text{N}_4$  (Table 1). These include: (1) texture and morphological modification of  $g\text{-C}_3\text{N}_4$ ; (2) doping of  $g\text{-C}_3\text{N}_4$  using of cations [noble metals: gold (Au), platinum (Pt), and silver (Ag) and transition metal: copper (Cu), nickel (Ni), iron (Fe) and strontium (Sn)] and anions [sulfur (S), carbon (C), fluorine (F), boron (B) and



phosphorous (P)]; and (3) incorporation of g-C<sub>3</sub>N<sub>4</sub> with suitable semiconductor materials [e.g., TiO<sub>2</sub>, CuO, AgX (X = Br, Cl and I), ZnO and GO]. These methods focus on reducing the energy band gap and extend visible light absorption, thus promoting photocatalytic disinfection. Table 2 lists notable recent works on g-C<sub>3</sub>N<sub>4</sub> composites for disinfection of microbial species.

### Texture and morphological modified g-C<sub>3</sub>N<sub>4</sub>-based composites

High surface area photocatalysts possess more surface reactive sites, improved charge transfer efficiency, and accelerated charge carrier separation efficiency; this enhances photocatalytic activity. For instance, Huang et al. [78] showed that *E. coli* K-12 can be efficiently destroyed with the existence of mesoporous g-C<sub>3</sub>N<sub>4</sub>, reaching 100% inactivation efficiency after 4-h visible light radiation. They also reported that the surface area of mesoporous g-C<sub>3</sub>N<sub>4</sub> is 20 times greater than bulk g-C<sub>3</sub>N<sub>4</sub> and photogenerated holes on g-C<sub>3</sub>N<sub>4</sub> surface can facilitate bacterial inactivation [78]. Simultaneously, visible light active high surface area (190 m<sup>2</sup> g<sup>-1</sup>) porous g-C<sub>3</sub>N<sub>4</sub> nanosheets (PCNS) could completely kill *E. coli* within 4 h, while bulk g-C<sub>3</sub>N<sub>4</sub> could kill 77.1% of *E. coli* cells [79]. Recently, Kang et al. [80] fabricated visible light active porous g-C<sub>3</sub>N<sub>4</sub> NS by two different approaches: alternated heating and cooling, and bacterial-inspired liquid exfoliation method. Porous g-C<sub>3</sub>N<sub>4</sub> NS gave better water disinfection behavior with respect to disinfection of *E. coli* as a result of its large surface area, low bandgap and, better electron transport ability [80]. Thurston et al. [27] evaluated the biocidal activity of urea and dicyandiamide and derived two different kinds of g-C<sub>3</sub>N<sub>4</sub> films against both G<sup>-</sup> (*E. coli*) and G<sup>+</sup> (*S. aureus*) bacteria [28]. Enhanced activity of u-g-C<sub>3</sub>N<sub>4</sub> on pathogenic organisms was explained to occur due to the factors such as high surface area (72.2 m<sup>2</sup> g<sup>-1</sup>), reduced band gap energy (2.86 ± 0.14 eV) and efficient separation of photogenerated electron–hole pairs. Notably, no antimicrobial activity was noticed for both g-C<sub>3</sub>N<sub>4</sub> films under dark conditions.

Delamination of pristine g-C<sub>3</sub>N<sub>4</sub> can improve photodisinfection activity. Bacteria-etched g-C<sub>3</sub>N<sub>4</sub> photocatalysts demonstrated four times enhanced photocatalytic water disinfection activity as compared with pristine g-C<sub>3</sub>N<sub>4</sub> and showed outstanding

stability under visible light exposure [53]. Functionalization of carboxyl (–COOH) and carbonyl (C=O) groups at the edge of g-C<sub>3</sub>N<sub>4</sub> can significantly promote *E. coli* inactivation efficiency of log<sub>10</sub>(C/C<sub>0</sub>) = 6 (> 99.9999%) under visible light exposure over a period of 30 min with lower catalyst consumption. Also, edge-functionalized g-C<sub>3</sub>N<sub>4</sub> nanosheets can effectively promote separation of charge carriers, stimulate upward surface band bending and assist production of H<sub>2</sub>O<sub>2</sub>, thus improving disinfection efficiency [58].

Also, urea-derived g-C<sub>3</sub>N<sub>4</sub> showed sporicidal activity against *Bacillus anthracis* (*B. anthracis*) endospores upon exposure to visible light. Nearly, 2 × 10<sup>7</sup> CFU mL<sup>-1</sup> of *E. coli* was destroyed totally using a visible active single-layered g-C<sub>3</sub>N<sub>4</sub> in a period of 4 h. g-C<sub>3</sub>N<sub>4</sub> nanosheet and g-C<sub>3</sub>N<sub>4</sub> (g-C<sub>3</sub>N<sub>4</sub> NS) reduced ~ 5 log and ~ 3 log of *E. coli*, respectively under similar experimental conditions [81]. Inactivation of MS2 phage using g-C<sub>3</sub>N<sub>4</sub> was first studied by Li and et al. [82]. Almost all viral species (1 × 10<sup>8</sup> PFU mL<sup>-1</sup>) could be completely killed in a period of around 6 h. Then, Zhang et al. [83] optimized the effect of different operating parameters such as light intensity, metal loading and, reaction temperature for inactivation of bacteriophage MS2 using response surface methodology (RSM) (Fig. 8). Up to 6.58 log PFU mL<sup>-1</sup> of viruses were inactivated under the optimized conditions of light intensity (199.8 mW cm<sup>-2</sup>), metal loading (135.4 mg L<sup>-1</sup>) and reaction temperature (24.05 °C), which is well matched with the experimental value (6.51 log PFU mL<sup>-1</sup>) [83].

### Anions (nonmetal) and cation (metal)-doped g-C<sub>3</sub>N<sub>4</sub>-based nanocomposites

Transition metal ions and noble metals are commonly employed as dopants to enhance photocatalytic disinfection efficiency. A transition metal can create an extra energy level within the semiconductor material, assisting the formation of electron–hole pairs and broadening spectral absorption toward the visible region. Electrons moving from one of these levels to CB require lesser photon energy than unmodified semiconductors. Numerous transition metal-doped g-C<sub>3</sub>N<sub>4</sub> have been reported for photocatalytic applications. But, none of them report its potential for photocatalytic disinfection of microbes. Noble metals incorporated g-C<sub>3</sub>N<sub>4</sub> photocatalysts can enhance the photocatalytic performance by creating charge

**Table 2** Photocatalytic disinfection efficiency of g-C<sub>3</sub>N<sub>4</sub>-based composites

Catalyst	Synthesis method	Target microorganism name/ load (bacteria and algae) (CFU mL <sup>-1</sup> ) and virus (PFU/ mL)	Inactivation time (min)	Activity		ROS	References
				In dark	In light		
Pristine and texture and morphological modification of g-C <sub>3</sub> N <sub>4</sub> Mesoporous g-C <sub>3</sub> N <sub>4</sub>	Template assisted	<i>E. coli</i> K-12/2.5 × 10 <sup>6</sup>	240	No	Yes (300 W Xe lamp with λ < 400 nm filter)	h <sup>+</sup>	[78]
	Hydrothermal and thermal etching	<i>E. coli</i> /5 × 10 <sup>6</sup>	240	Limited (14.5%)	Yes (500 W Xe lamp with λ = 420 nm filter)	·O <sub>2</sub> <sup>-</sup> and h <sup>+</sup>	[79]
g-C <sub>3</sub> N <sub>4</sub> nanosheets	microwave-assisted ACHT (alternate heating and cooling treatment) method	<i>E. coli</i> /2.5 × 10 <sup>7</sup>	120	–	Yes (300 W Xe lamp with λ > 420 nm filter)	·O <sub>2</sub> <sup>-</sup> and ·OH	[80]
Bacteria-treated g-C <sub>3</sub> N <sub>4</sub> (BT-CN)	Bacterial-inspired liquid exfoliation method	<i>E. coli</i> /2 × 10 <sup>7</sup>	120	–	Yes (300 W Xe lamp with 420 nm filter)	·O <sub>2</sub> <sup>-</sup> and ·OH	[53]
Edge-functionalized g-C <sub>3</sub> N <sub>4</sub> nanosheets	Facile wet chemical method	<i>E. coli Salmonella</i> (1 × 10 <sup>6</sup> )	30	–	Yes (300 W Xe lamp with λ > 400 nm filter)	H <sub>2</sub> O <sub>2</sub>	[58]
u-g-C <sub>3</sub> N <sub>4</sub> films	Calcination	<i>S. aureus</i> ATCC#6538 (methicillin sensitive)	7.8	No	Yes (270 W Xe lamp with λ = 400 nm filter)	·OH	[27]
		<i>S. aureus</i> (methicillin resistant)	6				
		<i>E. coli</i> O157:H7	2.4				
		<i>B. anthracis endospores</i> (Sterne 34F2)/14–15 CFU/ cm <sup>2</sup>	35.4				
Nanostructured g-C <sub>3</sub> N <sub>4</sub> (ns- g-C <sub>3</sub> N <sub>4</sub> )	Exfoliation	<i>E. coli</i> O157:H7/ 11.4 CFU cm <sup>-2</sup> and <i>S.</i> <i>aureus</i> /14.4 CFU cm <sup>-2</sup>	54.6	No	Yes (270 W Xe lamp with λ = 400 nm filter)	·OH	[28]
Single-layer g-C <sub>3</sub> N <sub>4</sub>	Thermal etching and ultrasonic exfoliation	<i>E. coli</i> /2 × 10 <sup>7</sup>	240	No	Yes (500 W Xe lamp, with λ > 400 nm filter)	h <sup>+</sup>	[81]
Bulk g-C <sub>3</sub> N <sub>4</sub>	Direct heating	<i>Bacteriophage MS2</i> /1 × 10 <sup>8</sup>	360	No	Yes (300 W Xe lamp, λ ≥ 400 nm filter)	·O <sub>2</sub> <sup>-</sup> and ·OH	[82]
Bulk g-C <sub>3</sub> N <sub>4</sub>	Two-step heat treatment	<i>Bacteriophage MS2</i> /1 × 10 <sup>8</sup>	240	No	Yes (300 W Xe lamp, with 400 nm filter)	·O <sub>2</sub> <sup>-</sup> and ·OH	[83]
Influence of anions (metal) and cation (nonmetal) doping Ag/g-C <sub>3</sub> N <sub>4</sub>	Sonication	<i>E. coli, S. aureus</i> /1 × 10 <sup>6</sup>	30	No	Yes (300 W halogen lamp)	–	[89]
		<i>S. aureus</i> bio film	180				
Ag/g-C <sub>3</sub> N <sub>4</sub>	Photoassisted reduction method	<i>E. coli</i> /1 × 10 <sup>9</sup>	90	No	Yes (300 W Xe lamp with λ < 420 nm filter)	·O <sub>2</sub> <sup>-</sup> and h <sup>+</sup>	[90]

Table 2 continued

Catalyst	Synthesis method	Target microorganism name/ load (bacteria and algae) (CFU mL <sup>-1</sup> ) and virus (PFU/ mL)	Inactivation time (min)	Activity		ROS	References
				In dark	In light		
g-C <sub>3</sub> N <sub>4</sub> /Ag	One-pot green synthesis method	<i>E. coli</i> , <i>P. aeruginosa</i> , <i>S. aureus</i> and <i>B. subtilis</i>	–	Yes	–	–	[92]
Ag/g-C <sub>3</sub> N <sub>4</sub>	Hydrothermal and photoassisted reduction	<i>S. aureus</i> /1 × 10 <sup>7</sup>	180	No	Yes (500 W Xe lamp with 420 nm filter)	·O <sub>2</sub> <sup>-</sup> and <i>h</i> <sup>+</sup>	[91]
Ag-g-C <sub>3</sub> N <sub>4</sub>	Single-pot microemulsion preparation method	<i>E. coli</i> 1337-H/8.9 × 10 <sup>9</sup>	60	Low	Yes (UV light (385 nm) and visible light (515 nm))	·OH	[93]
Au/g-C <sub>3</sub> N <sub>4</sub>	Deposition–precipitation method	<i>E. coli</i> , <i>S. aureus</i> , <i>B. subtilis</i> and <i>S. epidermidis</i> /1 × 10 <sup>6</sup>	30	Yes	–	·OH	[94]
g-C <sub>3</sub> N <sub>4</sub> /red P hybrid nanosheets	Ultrasonic-assisted wet chemical method	<i>E. coli</i> /1 × 10 <sup>7</sup>	120	No	Yes (300 W Xenon lamp)	<i>h</i> <sup>+</sup> , ·O <sub>2</sub> <sup>-</sup> and H <sub>2</sub> O <sub>2</sub>	[95]
Incorporation of g-C <sub>3</sub> N <sub>4</sub> with other semiconductor materials							
(a) Binary							
g-C <sub>3</sub> N <sub>4</sub> /TiO <sub>2</sub>	Hydrothermal calcination	<i>E. coli</i> K-12/(1 × 10 <sup>7</sup> )	180	No	Yes (300 W Xe lamp, λ > 420 nm filter)	<i>h</i> <sup>+</sup> , ·O <sub>2</sub> <sup>-</sup> and H <sub>2</sub> O <sub>2</sub>	[96]
g-C <sub>3</sub> N <sub>4</sub> /TiNT	Chemical vapor deposition	<i>E. coli</i> DH5α/1 × 10 <sup>5</sup>	180	No	Yes (300 W Xe lamp λ < 420 nm filter)	·OH	[97]
g-C <sub>3</sub> N <sub>4</sub> QDs/TNA (titanium nanotube array)	Electrochemical anodization	<i>E. coli</i>	180	No	Yes (500 W Xe lamp)	·O <sub>2</sub> <sup>-</sup>	[98]
HT-CN/TiO <sub>2</sub>	Hydrothermal method	<i>E. coli</i> /1 × 10 <sup>3</sup>	30	Yes (low)	Yes (300 W Xe lamp with 1.5 AM filter)	O <sub>2</sub> <sup>-</sup> and ·OH	[99]
Bi <sub>2</sub> MoO <sub>6</sub> /g-C <sub>3</sub> N <sub>4</sub> NSs	In situ solvothermal	<i>E. coli</i> DH5α/2.5 × 10 <sup>7</sup>	150	No	Yes (300 W Xenon lamp with λ > 420 nm filter)	<i>h</i> <sup>+</sup>	[100]
g-C <sub>3</sub> N <sub>4</sub> /m-Bi <sub>2</sub> O <sub>4</sub>	Hydrothermal method	<i>E. coli</i> K-12/1 × 10 <sup>6</sup>	90	–	Yes (300 W Xe lamp, cut of filter λ < 400 nm)	<i>h</i> <sup>+</sup> , ·O <sub>2</sub> <sup>-</sup> and H <sub>2</sub> O <sub>2</sub>	[101]
g-C <sub>3</sub> N <sub>4</sub> -AgBr	Adsorption–deposition method	<i>E. coli</i> ATCC15597 <i>S. aureus</i> ATCC6538/ 3 × 10 <sup>6</sup>	60 150	No	Yes (300 W Xe lamp with 400 nm filter)	<i>h</i> <sup>+</sup>	[102]
Ag <sub>2</sub> WO <sub>4</sub> /g-C <sub>3</sub> N <sub>4</sub>	Deposition–precipitation method	<i>E. coli</i> /1 × 10 <sup>7</sup>	90	No	Yes (300 W Xe lamp with λ < 420 nm filter)	<i>h</i> <sup>+</sup> , ·O <sub>2</sub> <sup>-</sup> and ·OH	[103]
(AgVO <sub>3</sub> , BiVO <sub>4</sub> ) QDs/g- C <sub>3</sub> N <sub>4</sub>	Ultrasonication method	<i>Salmonella</i> H9812/1 × 10 <sup>7</sup>	10.2	No	Yes (300 W Xe lamp with λ > 400 nm filter)	·O <sub>2</sub> <sup>-</sup>	[104]

Table 2 continued

Catalyst	Synthesis method	Target microorganism name/ load (bacteria and algae) (CFU mL <sup>-1</sup> ) and virus (PFU/ mL)	Inactivation time (min)	Activity		ROS	References
				In dark	In light		
Ni <sub>2</sub> P/g-C <sub>3</sub> N <sub>4</sub>	One-pot hydrothermal method	<i>E. coli</i> K-12/1 × 10 <sup>7</sup>	240	Yes (low)	Yes (300 W Xe lamp λ = 420 nm filter)	h <sup>+</sup> and H <sub>2</sub> O <sub>2</sub>	[105]
g-C <sub>3</sub> N <sub>4</sub> /CdCO <sub>3</sub>	Microwave heating method	<i>E. coli</i> /1 × 10 <sup>5</sup>	45	Yes (low)	Yes (200 W tungsten lamp)	·OH and ·O <sub>2</sub> <sup>-</sup>	[106]
ZnO/g-C <sub>3</sub> N <sub>4</sub>	Thermal condensation	<i>E. coli</i> ATCC 52922 and <i>S. aureus</i> ATCC 29231/1 × 10 <sup>8</sup>	NA	Yes	–	–	[107]
Graphene oxide/g-C <sub>3</sub> N <sub>4</sub>	Sonochemical method	<i>E. coli</i> /1 × 10 <sup>7</sup>	120	No	Yes (300 W Xe lamp with λ < 420 nm filter)	h <sup>+</sup>	[109]
CNRGOS8 RGOCNS8	NA	<i>E. coli</i> K-12/2 × 10 <sup>6</sup>	240	No	Yes (300 W Xe lamp with λ < 400 nm filter)	·O <sub>2</sub> <sup>-</sup> , ·OH and H <sub>2</sub> O <sub>2</sub>	[110]
C60/C <sub>3</sub> N <sub>4</sub> and C70/C <sub>3</sub> N <sub>4</sub>	Hydrothermal	<i>E. coli</i> O157:H7/0.5 mg L <sup>-1</sup>	240	No	Yes (300 W Xe lamp with λ > 420 nm filter)	·O <sub>2</sub> <sup>-</sup> and ·OH	[111]
g-C <sub>3</sub> N <sub>4</sub> /EP	Facile thermal method	<i>E. coli and</i> MS2 phage/1 × 10 <sup>8</sup>	180 240	No	Yes (300 W Xe lamp with 400 nm filter)	·O <sub>2</sub> <sup>-</sup> and ·OH	[112]
(b) Tertiary g-C <sub>3</sub> N <sub>4</sub> /Ag/TiO <sub>2</sub>	Two-nozzle electrospinning– calcination	<i>E. coli</i> ATCC 52922 and <i>S. aureus</i> ATCC 29231/1 × 10 <sup>7</sup>	480	Yes	Yes (natural light)	–	[113]
Ag-ZnO/g-C <sub>3</sub> N <sub>4</sub>	Hydrothermal method	<i>E. coli</i> /1 × 10 <sup>6</sup>	120	Yes	Yes (mercury vapor lamp)	–	[114]
Ag-Fe <sub>3</sub> O <sub>4</sub> /g-C <sub>3</sub> N <sub>4</sub>	Hydrothermal	<i>E. coli</i> /1 × 10 <sup>7</sup>	120	Yes	–	–	[115]
Ag/AgO/g-C <sub>3</sub> N <sub>4</sub> microsphere	Thermal heating	<i>E. coli</i> ATCC 25933/1 × 10 <sup>5</sup>	30	Low	Yes (100 W tungsten lamp)	h <sup>+</sup> and H <sub>2</sub> O <sub>2</sub>	[116]
Ag/g-C <sub>3</sub> N <sub>4</sub> /PES membranes	Phase-inversion method	<i>E. coli, P. aeruginosa</i>	–	Yes	–	–	[117]
g-C <sub>3</sub> N <sub>4</sub> -Bi <sub>2</sub> MoO <sub>6</sub> -Ag	Hydrothermal method	<i>E. coli and S. aureus</i>	–	Yes	Yes	–	[26]
BiVO <sub>4</sub> /Ag/g-C <sub>3</sub> N <sub>4</sub>	Photodeposition and hydrothermal reactions	<i>E. coli</i> /3 × 10 <sup>6</sup>	60	No	Yes (compact fluorescent lamps)	·O <sub>2</sub> <sup>-</sup> , ·OH and H <sub>2</sub> O <sub>2</sub>	[118]
B/Phenyl/g-C <sub>3</sub> N <sub>4</sub>	Thermal polycondensation	<i>E. coli</i> /5 × 10 <sup>5</sup>	180	No	Yes (300 W Xe lamp, with λ > 420 nm filter)	·O <sub>2</sub> <sup>-</sup> and H <sub>2</sub> O <sub>2</sub>	[119]
g-C <sub>3</sub> N <sub>4</sub> /BiOI/BiOBr	Deposition–precipitation	<i>E. coli</i> ATCC 15597/1 × 10 <sup>3</sup>	180	No	Yes (300 W Xe lamp with λ < 400 nm filter)	·O <sub>2</sub> <sup>-</sup> , h <sup>+</sup> and ·OH	[120]



Table 2 continued

Catalyst	Synthesis method	Target microorganism name/ load (bacteria and algae (CFU mL <sup>-1</sup> ) and virus (PFU/ mL)	Inactivation time (min)	Activity		ROS	References
				In dark	In light		
P <sub>3</sub> C/CaO/g-C <sub>3</sub> N <sub>4</sub>	–	<i>E. coli</i> , <i>P. aeruginosa</i> , and <i>C. albicans</i> /1 × 10 <sup>5</sup>	–	Yes	–	–	[121]
g-C <sub>3</sub> N <sub>4</sub> /N <sub>2</sub> Ss/RGO/CA	Vacuum filtration	<i>E. coli</i> /3.5 × 10 <sup>6</sup>	300	–	Yes (300 W Xe lamp λ = 400 nm filter)	–	[122]
g-C <sub>3</sub> N <sub>4</sub> /Bi <sub>2</sub> MoO <sub>6</sub> /PEVE	Sonochemical	NA	240	–	Yes (500 W Xe lamp λ > 420 nm filter)	h <sup>+</sup> and ·O <sub>2</sub> <sup>-</sup>	[123]
g-C <sub>3</sub> N <sub>4</sub> -SnO <sub>2</sub> /TiO <sub>2</sub> NTs/Ti plates	Tipping and annealing	<i>E. coli</i> /1.5 × 10 <sup>8</sup>	60	No	Yes (Xe lamp λ > 350 nm (UV source) and λ > 420 nm (visible source) filter)	–	[124]
g-C <sub>3</sub> N <sub>4</sub> /TiO <sub>2</sub> /kaolinite	Sol-gel method associated with chemical stripping and self-assembly	<i>S. aureus</i> /1 × 10 <sup>7</sup>	300	No	Yes (8 W fluorescent lamp)	·O <sub>2</sub> <sup>-</sup>	[125]
g-C <sub>3</sub> N <sub>4</sub> /Al <sub>2</sub> O <sub>3</sub> /EP	Facile impregnation and calcination	<i>Microcystis aeruginosa</i> / 2.7 × 10 <sup>6</sup>	360	–	Yes (500 W Xe lamp λ = 400 nm filter)	·O <sub>2</sub> <sup>-</sup> and ·OH	[126]
g-C <sub>3</sub> N <sub>4</sub> /TiO <sub>2</sub> /Al <sub>2</sub> O <sub>3</sub> /EP	Sol-gel	<i>Microcystis aeruginosa</i> / 2.7 × 10 <sup>6</sup>	360	–	Yes (500 W Xe lamp with 400 nm filter)	h <sup>+</sup> and ·OH	[127]
g-C <sub>3</sub> N <sub>4</sub> /NP-TiO <sub>2</sub> /EGC	One-step sol-carbonization method	<i>Microcystis aeruginosa</i> / 2.7 × 10 <sup>6</sup>	60	–	Yes (500 W Xe lamp with 400 nm filter)	·O <sub>2</sub> <sup>-</sup> , h <sup>+</sup> and ·OH	[128]

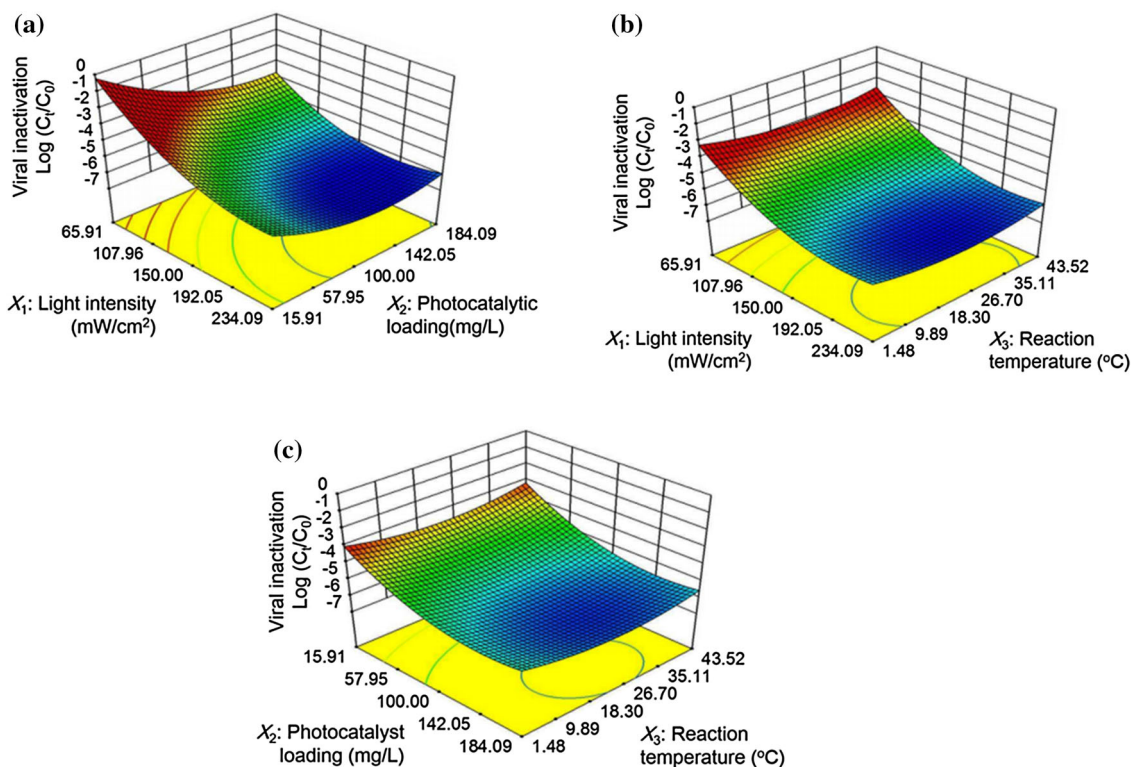


**Figure 8** a The 3D response surface plots of the photocatalytic viral inactivation efficiency by  $g\text{-C}_3\text{N}_4$  for interaction between a light intensity  $X_1$  and photocatalyst loading  $X_2$ , b light intensity

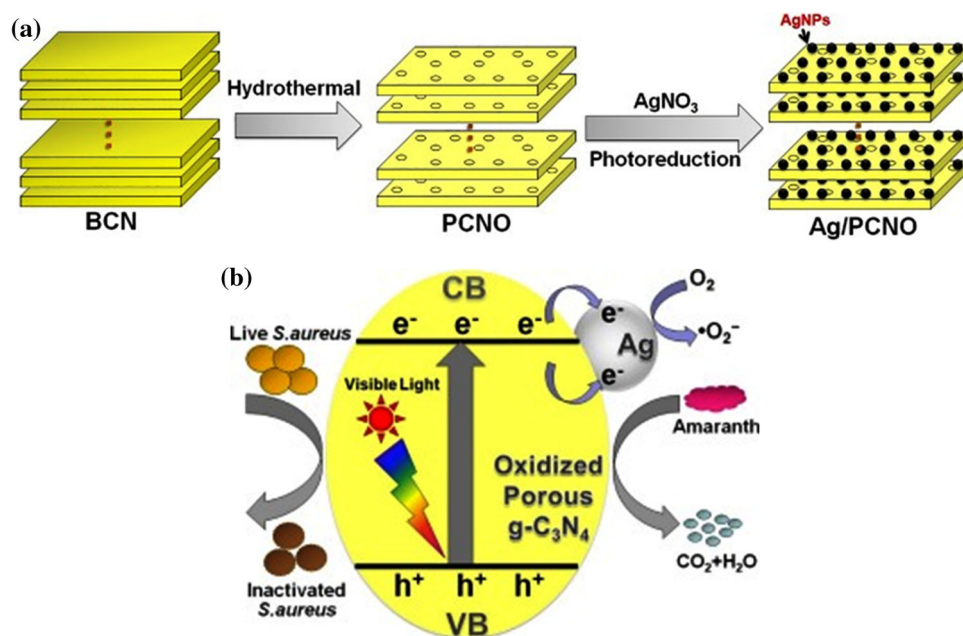
$X_1$  and reaction temperature  $X_3$  and c photocatalyst loading  $X_2$  and reaction temperature  $X_3$  [83].

carriers and extending its spectral absorption into visible region. In addition, surface plasmon resonance (SPR) effect of metal species can induce generation of charge carriers in  $g\text{-C}_3\text{N}_4$  [84–86]. Also, noble metals can behave as an electron sink for tapping free electrons, promoting the separation of photogenerated charge carriers and enhancing the photocatalytic efficiency of  $g\text{-C}_3\text{N}_4$  [87, 88]. i.e., Photogenerated electrons move from the CB of  $g\text{-C}_3\text{N}_4$  to the metal nanoparticle deposited on  $g\text{-C}_3\text{N}_4$  surface, while the photogenerated hole remains on  $g\text{-C}_3\text{N}_4$ . This leads to effective separation of photogenerated charge carriers and associated improvement of photocatalytic disinfection performance by the generation of ROS species.

Ag is a well-known bactericidal agent under dark condition. Sorption of Ag on negatively charged cell wall deactivates cellular enzymes, disturbs bacterial cell wall (membrane), and eventually causes cell lysis and cell death. Enhanced generation of ROS species on  $\text{Ag}/g\text{-C}_3\text{N}_4$  nanohybrids surface exhibited higher efficiency to inactivate bacterial species and better ability to destruct biofilms into proteins, nucleic

acids, and polysaccharides, when matched with  $g\text{-C}_3\text{N}_4$  nanosheets, in the presence of visible light [89]. Further, the hybrid effect of  $\text{Ag}/g\text{-C}_3\text{N}_4$  composite could extend visible light utilization efficiency, reduce recombination of charge carriers, promote fast separation and shifting of photogenerated charge carriers, and provide longer lifetime to charge carriers. A hybrid  $\text{Ag}/g\text{-C}_3\text{N}_4$  composite was fabricated by photoreduction approach, exhibiting acceptable disinfection efficiency toward *E. coli*. It was confirmed through experiments with different chemical scavengers that  $e^-$ ,  $h^+$ , and  $\cdot\text{O}_2^-$  species play a key role in demolition of bacterial cell wall [90]. Xu et al. [91] reported efficient antimicrobial activity against *S. aureus* by Ag-doped  $g\text{-C}_3\text{N}_4$ , synthesized by a two different approach (hydrothermal treatment and photoassisted reduction) (Fig. 9). In 3 h exposure, nearly, 29.6% and 99.4% of bacterial cells were inactivated by  $g\text{-C}_3\text{N}_4$  and  $\text{Ag}/g\text{-C}_3\text{N}_4$  composites, respectively [91]. Besides,  $h^+$  and  $\text{O}_2^-$  species were observed to be significant species for bacterial inactivation with  $\text{Ag}/g\text{-C}_3\text{N}_4$  ( $\text{Ag}/\text{PCNO}$ ) in the photocatalysis process. Also, high efficiency of

**Figure 9** **a** Synthesis of Ag/g-C<sub>3</sub>N<sub>4</sub> composite and **b** generation and transfer of photogenerated charge carriers at the interface of Ag/g-C<sub>3</sub>N<sub>4</sub> under visible light irradiation [91].



Ag/PCNO was explained to occur because of SPR effect of AgNPs and the synergistic influence from PCNO molecules.

As compared to pure AgNP, one-pot green synthesis of g-C<sub>3</sub>N<sub>4</sub>/AgNPs nanocomposite using grape seed extract as the stabilizing agent displayed better bactericidal activity against *E. coli*, *P. aeruginosa*, *S. aureus*, and *B. subtilis* in the absence of light. This can be ascribed to many combinational factors. First, the existence of AgNPs on g-C<sub>3</sub>N<sub>4</sub> surface leads to bacterial species inactivation. Second, the incorporated g-C<sub>3</sub>N<sub>4</sub> and ligand molecules from grape extract interact with the surface of silver to make AgNPs highly stable. Also, g-C<sub>3</sub>N<sub>4</sub>/AgNPs nanocomposite is more compatible with G<sup>-</sup> bacteria than G<sup>+</sup> types [92]. Munoz-Batista et al. [93] demonstrated that Ag-doped g-C<sub>3</sub>N<sub>4</sub> (Ag-g-C<sub>3</sub>N<sub>4</sub>) nanocomposite significantly enhances antimicrobial performance against *E. Coli* under both UV as well as in the visible region. Nanocomposites exhibit improved bactericidal activity than AgNPs without g-C<sub>3</sub>N<sub>4</sub> because of better distribution and stability characteristics of AgNPs on g-C<sub>3</sub>N<sub>4</sub> surface.

Apart from Ag, integration of Au NPs with g-C<sub>3</sub>N<sub>4</sub> (CNA) can deliver outstanding peroxidase activity toward the breakdown of H<sub>2</sub>O<sub>2</sub> to ·OH radicals and can efficiently kill both G<sup>+</sup> and G<sup>-</sup> bacteria. Also, it shows good efficacy in breaking down existing DR biofilms and in suppressing the creation of fresh biofilms in vitro. Additionally, CNA has high toxicity

on cancer cells [94]. Importantly, the amount of metal loading can significantly enhance bactericidal activity. For instance, Bing et al. [89] observed enhanced antimicrobial activity at an optimum mass ratio of 1:10 Ag/g-C<sub>3</sub>N<sub>4</sub> nanohybrid with low concentration and with short illumination duration. Limited work on photocatalytic disinfection activity over nonmetal (N, S, C, etc.) doped g-C<sub>3</sub>N<sub>4</sub> is available. In one study, anchoring of red phosphorous (r-P) nanoparticle on g-C<sub>3</sub>N<sub>4</sub> nanosheets was observed to extend visible light absorption up to 700 nm, exhibiting higher photodisinfection activity than pure g-C<sub>3</sub>N<sub>4</sub> and r-P. Improved disinfection activity is mainly ascribed to type I band alignment between g-C<sub>3</sub>N<sub>4</sub> and r-P, which facilitates effective charge separation [95].

### Heterostructure-based g-C<sub>3</sub>N<sub>4</sub> nanocomposites

Hybridization of g-C<sub>3</sub>N<sub>4</sub> with other semiconductor materials is an attractive approach for enhancing its photocatalytic performance. The key advantages include: broadening absorption into visible region, effective separation of charge carriers by shifting electrons from higher CB to lower CB, and holes from higher VB to lower VB, preventing photocorrosion of semiconductor materials. Micron-sized TiO<sub>2</sub> spheres were enfolded with g-C<sub>3</sub>N<sub>4</sub> hybrid structure [(g-C<sub>3</sub>N<sub>4</sub>)/TiO<sub>2</sub>] by hydrothermal calcination approach and (g-C<sub>3</sub>N<sub>4</sub>)/TiO<sub>2</sub> hybrid material could completely

inactivate *E. coli* within 180 min under visible light exposure. Further, increase or decrease in hydrothermal temperature can alter photocatalytic inactivation efficiencies [96]. Xu et al. [97] described visible light activity of thin g-C<sub>3</sub>N<sub>4</sub> loaded on aligned surfaces of TiO<sub>2</sub> nanotube arrays (TiNT) for the removal of *E. coli*. Bacterial survival ratio of g-C<sub>3</sub>N<sub>4</sub>/TiNT and g-C<sub>3</sub>N<sub>4</sub> composites was ~ 16% and ~ 86%, respectively. Bactericidal results showed that 15 mg of melamine is the optimal precursor load for fabricating highest efficiency g-C<sub>3</sub>N<sub>4</sub>/TiNT layers. Also, bactericidal activity decreases under anaerobic conditions and no inactivation was observed in catalysts without exposure to light. Zhang and co-workers [98] demonstrated that g-C<sub>3</sub>N<sub>4</sub> quantum dots (QDs)-immobilized TiO<sub>2</sub> nanotube array (g-C<sub>3</sub>N<sub>4</sub> QDs/TNA) membrane showed an impressive performance for improved antifouling capacity during filtering water containing *E. coli* under visible light exposure. A vertical heterojunction with Z-scheme feature was achieved by conjoining g-C<sub>3</sub>N<sub>4</sub> and anatase TiO<sub>2</sub> with {001} facets by a hydrothermal process. The coupled band structure trigger enhanced photocatalytic antibacterial activity in contrast with physically prepared composites and pure g-C<sub>3</sub>N<sub>4</sub> and TiO<sub>2</sub> [99].

Of late, visible light active Bi-based semiconductor materials have gained extensive attention in photocatalysis owing to their unique crystalline structures and absorption characteristics in visible light. Photocatalytic disinfection activities of Bi<sub>2</sub>MoO<sub>6</sub>/g-C<sub>3</sub>N<sub>4</sub> NS<sub>s</sub> (BM/CNNs) composites are higher under visible light exposure. Further, photocatalytic disinfection activity of BM/CNNs composite was higher at optimum loading BM content of 20% (by weight) [100]. Z-scheme-type monoclinic dibismuth tetraoxide (m-g-C<sub>3</sub>N<sub>4</sub>/Bi<sub>2</sub>O<sub>4</sub>) heterojunction was fabricated through a facile hydrothermal approach by Xia et al. (2017). The optimal ratio (1:0.5) of m-g-C<sub>3</sub>N<sub>4</sub>/Bi<sub>2</sub>O<sub>4</sub> of composite could inactivated 6 log<sub>10</sub> CFU mL<sup>-1</sup> of *E. coli* K-12 for a period of 1.5 h of visible light exposure was more efficient than g-C<sub>3</sub>N<sub>4</sub> (1.5 log) and m-Bi<sub>2</sub>O<sub>4</sub> (4 log) [101]. Particularly, disinfection efficiency did not increase noticeably with increasing m-Bi<sub>2</sub>O<sub>4</sub> content, whereas excessive m-Bi<sub>2</sub>O<sub>4</sub> can act as the recombination center of photogenerated charge carrier thereby diminishing the separation efficiency of electron–hole pairs.

By modifying g-C<sub>3</sub>N<sub>4</sub> with plasmonic photocatalysts, the photocatalytic disinfection activity can be

improved to a significant extent. For instance, AgBr (photosensitive material)-coupled g-C<sub>3</sub>N<sub>4</sub> nanocomposite could inactivate 3 × 10<sup>6</sup> CFU mL<sup>-1</sup> of *E. coli* and *S. aureus* species in 60 min and 150 min, respectively. Generated h<sup>+</sup> and surface founded. OH on g-C<sub>3</sub>N<sub>4</sub>-AgBr surface are dominant ROS species that are responsible for bacterial inactivation. Moreover, bacterial disinfection efficiency is higher in alkaline environment owing to the generation of more surface found ·OH [102]. Photocatalytic disinfection activity of Ag<sub>2</sub>WO<sub>4</sub>/g-C<sub>3</sub>N<sub>4</sub> composite against *E. coli* was investigated by Li et al. [103]. Synthesized photocatalyst [Ag<sub>2</sub>WO<sub>4</sub> (5%)/g-C<sub>3</sub>N<sub>4</sub> composite] exhibited higher bactericidal efficiency than pure g-C<sub>3</sub>N<sub>4</sub> and Ag<sub>2</sub>WO<sub>4</sub> under visible light. Superior disinfection efficiency with reaction rate of 0.39 min<sup>-1</sup> was ascribed to the dispersion of Ag<sub>2</sub>WO<sub>4</sub> particles on g-C<sub>3</sub>N<sub>4</sub> surface. Enhanced charge separation rates in Ag<sub>2</sub>WO<sub>4</sub>(5%)/g-C<sub>3</sub>N<sub>4</sub> composite is also an important factor as indicated in Fig. 10 [103]. Due to unique benefits of small size, tunable optical property, and outstanding electron transfer rates, vanadate QDs have proven capabilities as photocatalysts for solar light harvesting. Incorporation of vanadate QDs (AgVO<sub>3</sub> and BiVO<sub>4</sub>) on g-C<sub>3</sub>N<sub>4</sub> surface can effectively promote its charge separation efficiency and thus result in improved photocatalytic disinfection. AgVO<sub>3</sub>/g-C<sub>3</sub>N<sub>4</sub> composite (0.75 mg mL<sup>-1</sup>) showed the superior bactericidal efficiency of 96.4% in 10 min due to the abundant generation of ROS in water [104]. In contrast, g-C<sub>3</sub>N<sub>4</sub> sample could inactivate only 54.13% of *Salmonella* spp. after 10 min treatment. Moreover, ·O<sub>2</sub><sup>-</sup> was the major ROS of themicrobial

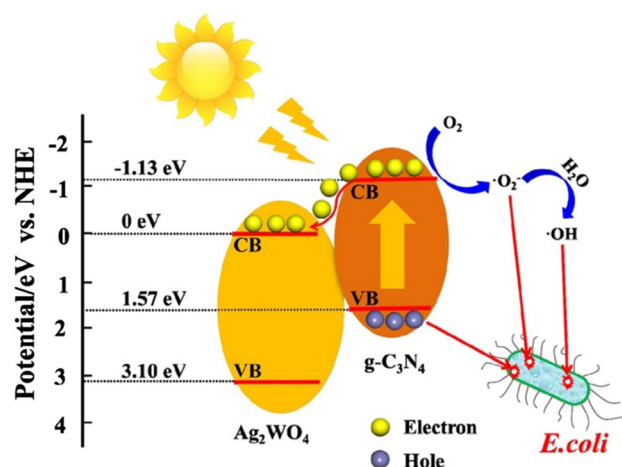


**Figure 10** Mechanism of photocatalytic disinfection treated with Ag<sub>2</sub>WO<sub>4</sub>/g-C<sub>3</sub>N<sub>4</sub> composite under visible light irradiation [103].



inactivation process. Also, the photocatalytic disinfection efficiency on *Salmonella* spp. was observed to be more effective as matched to *S. aureus* under same conditions. Particularly, photocatalysts made up of earth-abundant elements are preferred for microbial inactivation. Figure 11 shows the destruction *Salmonella* bacterial cell in  $\text{AgVO}_3$  QDs/ $\text{g-C}_3\text{N}_4$  at different exposure time under visible light.

Z-scheme type 10% $\text{Ni}_2\text{P}$ / $\text{g-C}_3\text{N}_4$  lamellar nanohybrids have been fabricated by hydrothermal synthesis using low-cost red phosphorous precursor and displayed 10 times faster inactivation under visible light exposure as compared with  $\text{g-C}_3\text{N}_4$ .  $\text{Ni}_2\text{P}$  could successfully trap photogenerated electrons and also facilitated  $h^+$  accumulation, leading to improved disinfection efficiency in case of *E. coli* K-12 [105]. Correspondingly, microwave in situ hybridization of organic  $\text{g-C}_3\text{N}_4$  with inorganic  $\text{CdCO}_3$  hybrid composite fully hindered the growth of *E. coli* bacteria within 45 min of visible light exposure at an optimum concentration of  $60 \mu\text{g mL}^{-1}$ . Nonetheless, higher catalyst loading restricted penetration of light into the suspension, thereby decreasing inactivation efficiency [106]. Sundaram et al. [107] synthesized  $\text{ZnO/g-C}_3\text{N}_4$  composite using single-step thermal condensation approach and tested its photocatalytic antimicrobial effect against *E. coli* and *S. aureus*. They demonstrated that  $\text{ZnO/g-C}_3\text{N}_4$  catalysts have good antimicrobial efficiency against *S. aureus* as compared to *E. coli*.

Recently, carbon-based composites have also been used as co-catalyst to facilitate transfer of electrons on  $\text{g-C}_3\text{N}_4$ . Also, 2D/2D nanocomposites facilitate better mobility of charge carrier across the heterojunction boundary, which in turn rise the charge carrier transfer and separation efficiency [108]. For example, coupling of 2D-structured  $\text{g-C}_3\text{N}_4$  with 2D-structured graphene oxide (GO) can improve photogenerated charge separation. Nearly 97.9% *E. coli* was killed by  $\text{GO/g-C}_3\text{N}_4$  composite with the concentration of  $100 \mu\text{g mL}^{-1}$  after 120 min of visible light exposure [109]. Moreover, Wang et al. (2013) fabricated  $\text{g-C}_3\text{N}_4$  (CN) sheets and reduced graphene oxide (RGO) wrapped on cyclo octasulfur ( $\alpha\text{-S}_8$ ) crystal ( $\text{CNRGOS}_8$  and  $\text{RGOCS}_8$ ) in two different orders and proved its antibacterial activity under both aerobic and anaerobic conditions.  $\text{CNRGOS}_8$  displayed superior photocatalytic disinfection activity than  $\text{RGOCS}_8$  under aerobic condition;  $\text{RGOCS}_8$  showed better photocatalytic performance under aerobic conditions as compared to  $\text{CNRGOS}_8$  composites [110]. Fullerene ( $\text{C}_{60}$  and  $\text{C}_{70}$ ) wrapped  $\text{g-C}_3\text{N}_4$  nanocomposites have been examined for bactericidal activity against *E. coli* O157:H7 bacteria under visible light exposure.  $\text{C}_{70}/\text{C}_3\text{N}_4$  composite demonstrated higher photocatalytic inactivation activity than  $\text{C}_{60}/\text{C}_3\text{N}_4$  composite ( $\sim 86\%$ ) within 4 h exposure to visible light [111]. On the contrary, bare  $\text{g-C}_3\text{N}_4$  inhibited only 68% bacterial cells after 4 h of visible light exposure. Correspondingly,  $\text{g-C}_3\text{N}_4/\text{EP}$  (porous

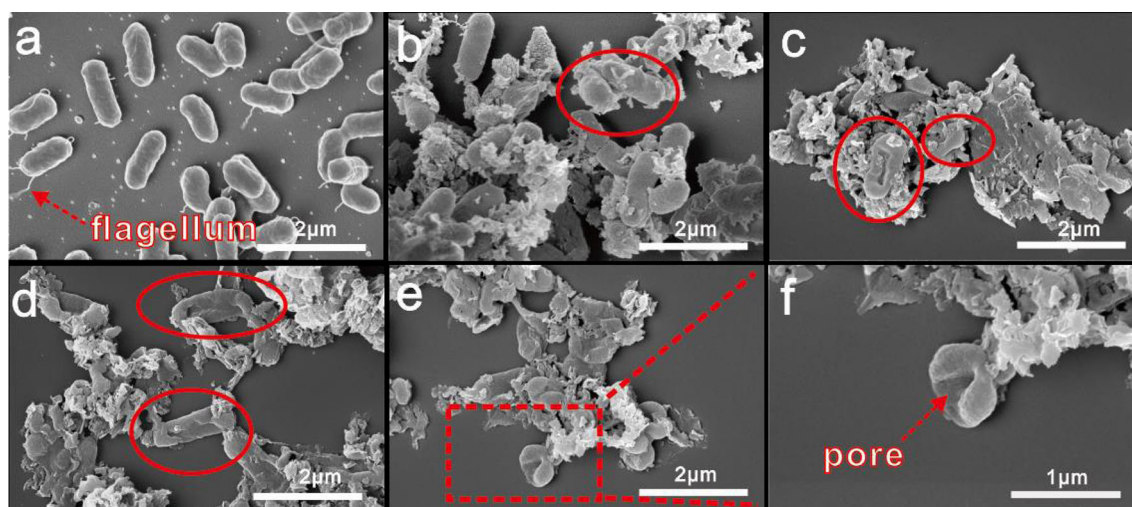
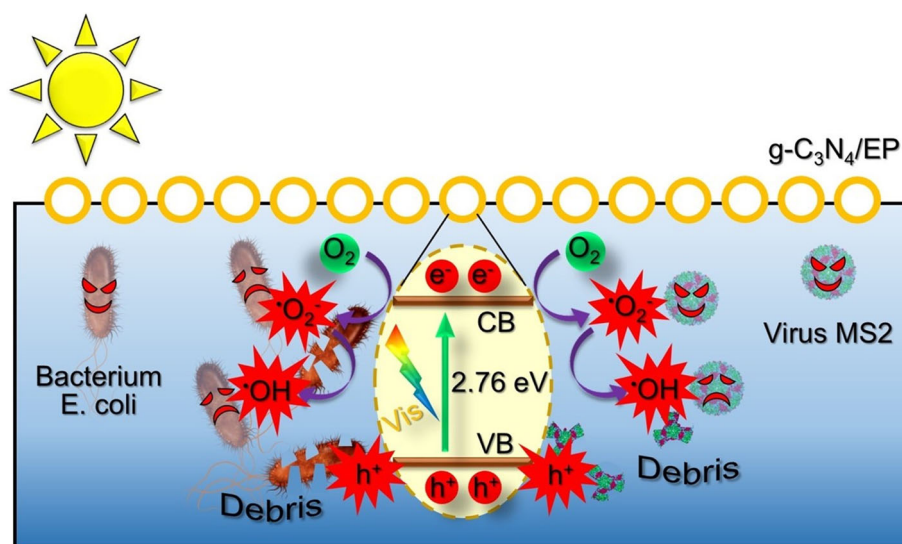


**Figure 11** SEM images of *Salmonella* ( $10^7$  CFU/mL) treated with  $\text{AgVO}_3/\text{g-C}_3\text{N}_4$  (0.75 mg/mL) under irradiation for **a** 0, **b** 5, **c** 10, **d** 20, **e** 30, **f** 30 min (magnified SEM image) [104].

**Figure 12** Proposed mechanism of bacterial and viral inactivation by g-C<sub>3</sub>N<sub>4</sub>/EP-520 under visible light irradiation [112].



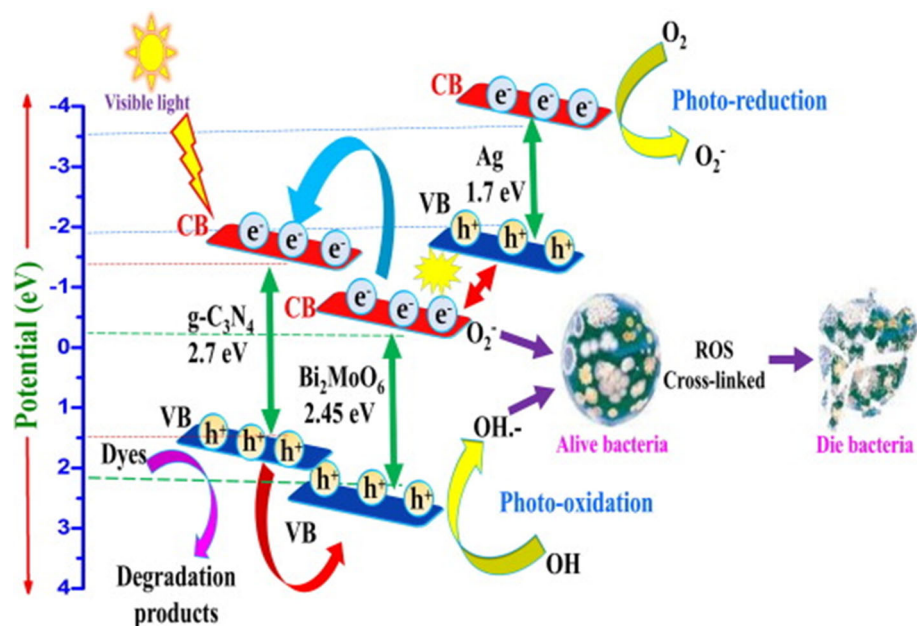
expanded perlite) composites exhibited excellent antibacterial activity against *E. coli* (8-log reduction) and antiviral activity (MS2 phage) in the absence of mechanical stirring under visible light exposure of 180 and 240 min, respectively (Fig. 12). Also, water quality parameters such as salinity (NaCl), hardness (Ca<sup>2+</sup>), dissolved oxygen (DO), and proton concentration can enhance the efficiency of g-C<sub>3</sub>N<sub>4</sub>/EP-520 for MS2 inactivation [112].

Loading of noble metals on g-C<sub>3</sub>N<sub>4</sub> hybrid composites can considerably improve its photocatalytic disinfection activity. For instance, Adhikari et al. (2016) recently developed ternary Ag-decorated TiO<sub>2</sub> NFs on g-C<sub>3</sub>N<sub>4</sub> sheet (Ag-TCN-5) using a two-nozzle electrospinning–calcination approach and showed high disinfection activity against both G<sup>-</sup> (*E. coli*) and G<sup>+</sup> (*S. aureus*) bacteria. The focus was on the released Ag ions that show enhanced antibacterial effects [113]. Similarly, distribution of Ag on ZnO/g-C<sub>3</sub>N<sub>4</sub> hybrid composites by one-pot hydrothermal method gave superior photocatalytic activity toward the degradation of MB and the antibacterial activity against *E. coli* was reported by Joo et al. [114]. Recently, Pant et al. [115] developed a novel, magnetically separable Ag-Fe<sub>3</sub>O<sub>4</sub>/g-C<sub>3</sub>N<sub>4</sub> composite by hydrothermal treatment. This showed superior photocatalytic activity toward *E. coli* bacteria. Then, facile thermal heating method fabrication of novel Ag/AgO-modified g-C<sub>3</sub>N<sub>4</sub> microspheres (Ag/AgO/g-CNMS) was used. The improved photocatalytic performance of Ag/AgO/g-CNMS is attributed to the collective effects of broadened light absorption and enhanced charge carrier separation efficiency. Further, 5 mg of 10% of Ag/

AgO/g-CNMS resulted in complete inactivation of *E. coli* within 0.5 h under visible light exposure [116]. Also, Zhang et al. [117] introduced Ag/g-C<sub>3</sub>N<sub>4</sub> nanosheets on polyethersulfone (PES) membrane by phase-inversion method. They observed that addition of Ag/g-C<sub>3</sub>N<sub>4</sub> nanosheets improved photocatalytic activity (degradation of methyl orange), antibacterial activity (*P. aeruginosa* and *E. coli*), and antifouling property. Likewise, g-C<sub>3</sub>N<sub>4</sub>-Bi<sub>2</sub>MoO<sub>6</sub>-Ag nanocomposite showed a higher antibacterial effect against both G<sup>+</sup> and G<sup>-</sup> bacterial species as shown in Fig. 13 [26]. Recently, Z-scheme BiVO<sub>4</sub>/Ag/g-C<sub>3</sub>N<sub>4</sub> ternary composites have been studied for improved photodisinfection activity against *E. coli* as compared with BiVO<sub>4</sub>/g-C<sub>3</sub>N<sub>4</sub> composite. Moreover, ternary composite showed lowered disinfection efficiency in case of sewage samples in contrast with that in synthetic saline solution due to the presence of natural organic matter (NOM) [118].

Graphitic carbon nitride-functionalized boron and phenyl (B/phenyl/g-C<sub>3</sub>N<sub>4</sub>) exhibited huge absorption range from ultraviolet light to near-infrared light. Nearly 99% *E. coli* were inhibited by B/phenyl/g-C<sub>3</sub>N<sub>4</sub> composites under visible light exposure for a duration of 180 min [119]. More interestingly, the photocatalytic antibacterial performance of g-C<sub>3</sub>N<sub>4</sub>/BiOI/BiOBr composite is obviously enhanced as compared to g-C<sub>3</sub>N<sub>4</sub> BiOI and BiOBr photocatalysts. Almost *E. coli* cells are completely killed under exposure of visible light for more than 3 h, whereas g-C<sub>3</sub>N<sub>4</sub>, BiOI, and BiOBr photocatalysts inactivated 83.7%, 34.2%, and 29.4% of *E. coli* cells within 5 h of treatment [120].

**Figure 13** Charge separation mechanism of the MB dye degradation and disinfection of bacteria over g-C<sub>3</sub>N<sub>4</sub>-Bi<sub>2</sub>MoO<sub>6</sub>-Ag tertiary composite [26].



Younis et al. [121] examined the removal of different dyes [methyl orange (MO), methylene blue (MB), and crystal violet (CV)] and antimicrobial activity of different pathogens (*E. coli*, *C. albicans* and *P. aeruginosa*) using CaO incorporated g-C<sub>3</sub>N<sub>4</sub>-based nanocomposites with 4,5-diphenyl-2-thioxo-2,5-dihydro-1H-pyrrole-3-carbonitrile (P<sub>3</sub>C@CaO-HCN) composite. They demonstrated that copolymer exhibited more affinity toward MB adsorption (1915.8  $\mu\text{mol g}^{-1}$ ), and antibacterial activity toward *E. coli* (93.5%), *C. albicans* (85.8%) and *P. aeruginosa* (61.54%) species. Superior antimicrobial effect was ascribed to the presence pyrrole-3-carbonitrile functionalized with cyanide (C≡N) and protonated g-C<sub>3</sub>N<sub>4</sub> (HCN) sheet [121].

In addition, integration of a membrane with the photocatalyst can efficiently mitigate membrane fouling as a result of efficient inactivation of microbial pollutants by photocatalysis. Assembling of g-C<sub>3</sub>N<sub>4</sub>NS/rGO photocatalyst on inexpensive cellulose acetate membrane via vacuum filtration method (namely g-C<sub>3</sub>N<sub>4</sub>NS/rGO/CA) could inactivate all bacteria (6.5 log reduction) under visible light in 2 h [122]. Also, incorporation of g-C<sub>3</sub>N<sub>4</sub>/Bi<sub>2</sub>MoO<sub>6</sub> into fluorocarbon resin (PEVE) can enhance photocatalytic sterilization performance of PEVE. The sterilization performance of composite coatings was prominent, when the amount of g-C<sub>3</sub>N<sub>4</sub> in Bi<sub>2</sub>MoO<sub>6</sub> was about 7%, under visible light irradiation for 4 h. Besides, g-C<sub>3</sub>N<sub>4</sub> enhanced charge transfer efficiency

of Bi<sub>2</sub>MoO<sub>6</sub> in the presence of visible light, and participated to the generation of more strong oxidizing species (O<sub>2</sub><sup>-</sup> and h<sup>+</sup>) [123]. Correspondingly, alteration of TiO<sub>2</sub> nanotubes/Ti plates with g-C<sub>3</sub>N<sub>4</sub>-SnO<sub>2</sub> composites lead to improved photocatalytic activity in two different systems (chemical and microbial). Better photocatalytic and bactericidal activity of g-C<sub>3</sub>N<sub>4</sub>-SnO<sub>2</sub>/TiO<sub>2</sub> nanotubes/Ti plate was ascribed to the efficient separation of electron-hole between g-C<sub>3</sub>N<sub>4</sub>-SnO<sub>2</sub> and TiO<sub>2</sub> nanotubes/Ti in the ternary composite. Further, these researchers studied the generation of CO<sub>2</sub> during bacterial species mineralization under visible light exposure (Fig. 14). Initially, the evolved CO<sub>2</sub> levels was unchanged and then gradually elevated with time, showing the restraint of bacteria breathing, followed by bacterial death [124].

The sandwich structure of g-C<sub>3</sub>N<sub>4</sub>/TiO<sub>2</sub>/kaolinite composite showed higher bactericidal efficiency against *S. aureus* in comparison with g-C<sub>3</sub>N<sub>4</sub>, TiO<sub>2</sub>, and kaolinite [125]. Song et al. [126, 127] fabricated two different nanocomposites: g-C<sub>3</sub>N<sub>4</sub> immobilized with Al<sub>2</sub>O<sub>3</sub>/EP (g-C<sub>3</sub>N<sub>4</sub>/Al<sub>2</sub>O<sub>3</sub>/EP) and both g-C<sub>3</sub>N<sub>4</sub> and TiO<sub>2</sub> immobilized Al<sub>2</sub>O<sub>3</sub>/EP (g-C<sub>3</sub>N<sub>4</sub>/TiO<sub>2</sub>/Al<sub>2</sub>O<sub>3</sub>/EP). Removal efficiency of *Microcystis aeruginosa* algal species ( $2.7 \times 10^6$  CFU mL<sup>-1</sup>) were 74.4% and 88.1% for g-C<sub>3</sub>N<sub>4</sub>/Al<sub>2</sub>O<sub>3</sub>/EP and g-C<sub>3</sub>N<sub>4</sub>/TiO<sub>2</sub>/Al<sub>2</sub>O<sub>3</sub>/EP, respectively after 6 h reaction [126, 127]. g-C<sub>3</sub>N<sub>4</sub> and nitrogen-phosphorus co-doped TiO<sub>2</sub> (named as AP-EGC-CT composite) hybridized with



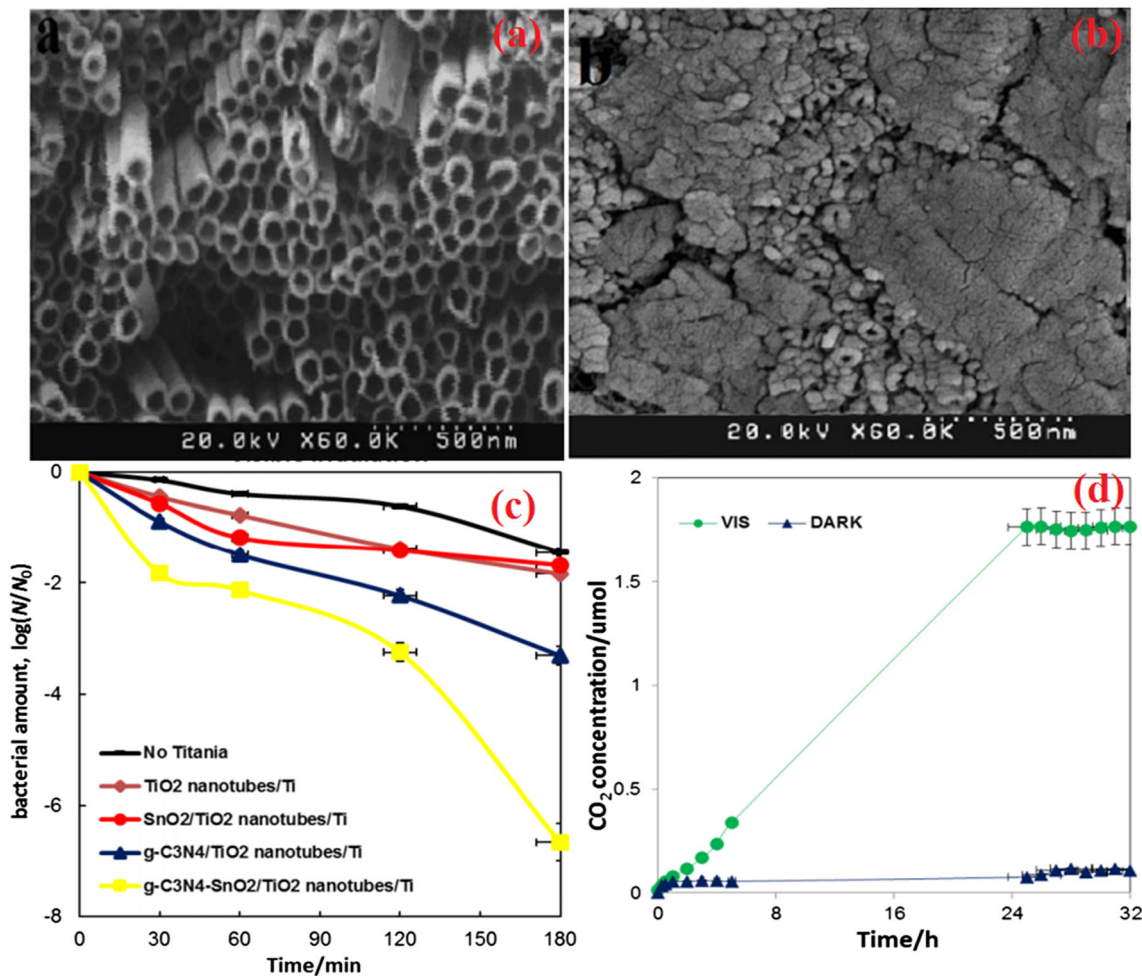


**Figure 14** SEM images of **a** bare TiO<sub>2</sub> nanotubes/Ti plate, **b** g-C<sub>3</sub>N<sub>4</sub>-SnO<sub>2</sub>/TiO<sub>2</sub> nanotubes/Ti plate and **c** antibacterial activity of fabricated plates for *E. coli* degradation under visible light

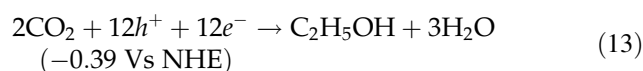
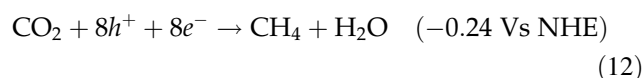
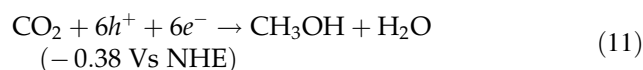
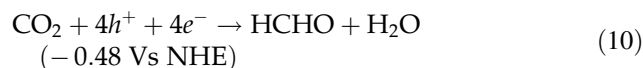
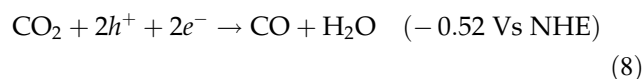
irradiation and **d** CO<sub>2</sub> evolution caused by mineralization of *E. coli* cells under visible light illumination and in the dark for 32 h [124].

functional expanded graphite covered carbon layer composites (AP-EGC) could remove 98.2% algal cells (*M. aeruginosa*) following 2 h treatment [128]. Algal cell inactivation was significantly facilitated by the photocatalytic oxidation process as shown in Fig. 15.

## Other applications

### CO<sub>2</sub> photoreduction

The energy band structure of g-C<sub>3</sub>N<sub>4</sub> is suitable for CO<sub>2</sub> photoreduction to sufficient number of value-added chemical fuels (CO, CH<sub>4</sub>, CH<sub>3</sub>OH, HCOOH and C<sub>2</sub>H<sub>5</sub>OH).



Difference in microstructure and crystallinity of g-C<sub>3</sub>N<sub>4</sub> leads to different kinds of products. For instance, urea-derived g-C<sub>3</sub>N<sub>4</sub> produces CH<sub>3</sub>OH and



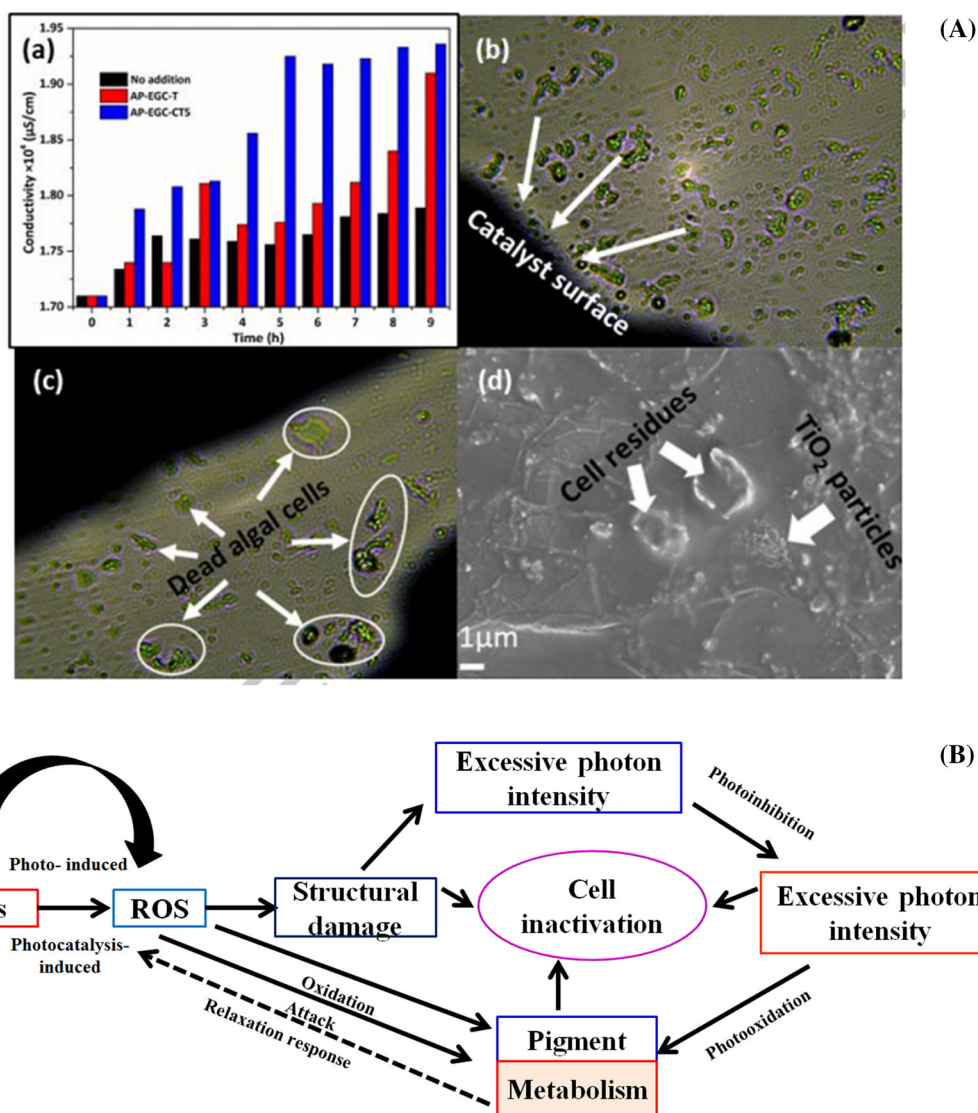


**Figure 15** **A** (a) Changes in conductivity during photocatalytic process; Microscopic images after (b) 15 min and (c) 3 h reaction and (d) SEM image after 9 h reaction; **B** Schematic diagram of the algal inactivation process [128].

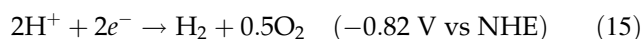
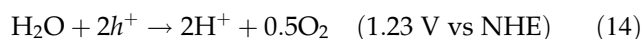
$\text{C}_2\text{H}_5\text{OH}$  from  $\text{CO}_2$ ; using melamine-derived  $\text{g-C}_3\text{N}_4$  only leads to the selective formation of  $\text{C}_2\text{H}_5\text{OH}$  (Mao et al. [43]). So far,  $\text{g-C}_3\text{N}_4$  with various nanostructures such as mesoporous structures, nanosheets, nanowires, and nanocomposites have been synthesized for enhanced  $\text{CO}_2$  photoreduction (Niu et al. [129]). Besides, it is explained that the amino groups of  $\text{g-C}_3\text{N}_4$  play a crucial role for the adsorption and activation of  $\text{CO}_2$  on its surface [130, 131]. Modification of electronic band structure and textural property of  $\text{g-C}_3\text{N}_4$  can improve its photocatalytic activity. Doping of metals (Cu, Pt, Mg and Mo) and nonmetal (S, P, r-P and O) on  $\text{g-C}_3\text{N}_4$  composites have been studied for  $\text{CO}_2$  photoreduction, as an approach to

provide a positive effect on reducing the charge carrier recombination and lower band gap energy, thus leading to superior photocatalytic activity toward the reduction of  $\text{CO}_2$  [42, 132–136]. Moreover, different Ru complexes,  $\text{trans}(\text{Cl})\text{-}[\text{Ru}(\text{bpyX}_2)(\text{CO})_2\text{Cl}_2]$  ( $\text{bpyX}_2 = 2,2'$ -bipyridine with substituents 'X' in the 4-positions,  $\text{X} = \text{H}$ ,  $\text{CH}_3\text{PO}_3\text{H}_2$  or  $\text{CH}_2\text{PO}_3\text{H}_2$ ), achieved enhanced photocatalytic activities of  $\text{CO}_2$  into  $\text{HCOOH}$  with high turnover number ( $> 1000$ ) (Kuriki et al. [137]). Integration of zero-dimensional carbon dots on 2D  $\text{g-C}_3\text{N}_4$  nanocomposites significantly influences the reduction of  $\text{CO}_2$  into value-added chemicals ( $\text{CH}_4$  and  $\text{CO}$ ). Besides 3 wt% of CND loading showed highest evolutions of  $\text{CH}_4$

(29.23  $\mu\text{mol}\cdot\text{g}\cdot\text{catalyst}^{-1}$ ) and CO (58.82  $\mu\text{mol}\cdot\text{g}\cdot\text{catalyst}^{-1}$ ) under visible light exposure after 10 h. The resultant apparent quantum efficiency (AQE) was 0.076% [138]. Increase in photoactivity using CN/D/pCN-3 was explained to be because of synergistic interaction between pCN and CNDs, allowing effective migration of photoexcited electrons from pCN to CNDs via well-contacted heterojunction interfaces which retard charge recombination. Likewise, several type II and Z-scheme g-C<sub>3</sub>N<sub>4</sub>-based heterojunctions have been evaluated for CO<sub>2</sub> photoreduction; examples include: TiO<sub>2</sub>/g-C<sub>3</sub>N<sub>4</sub>, LaPO<sub>4</sub>/g-C<sub>3</sub>N<sub>4</sub>, B<sub>4</sub>C/g-C<sub>3</sub>N<sub>4</sub>, In<sub>2</sub>O<sub>3</sub>/g-C<sub>3</sub>N<sub>4</sub>, g-C<sub>3</sub>N<sub>4</sub>/NaNbO<sub>3</sub>, g-C<sub>3</sub>N<sub>4</sub>/ZIF-8, CdIn<sub>2</sub>S<sub>4</sub>/mpg-C<sub>3</sub>N<sub>4</sub>, g-C<sub>3</sub>N<sub>4</sub>/NiAl-LDH, Ag<sub>3</sub>PO<sub>4</sub>/g-C<sub>3</sub>N<sub>4</sub>, SnO<sub>2</sub>x/g-C<sub>3</sub>N<sub>4</sub>, ZnO/g-C<sub>3</sub>N<sub>4</sub>, g-C<sub>3</sub>N<sub>4</sub>/Bi<sub>2</sub>WO<sub>6</sub>, g-C<sub>3</sub>N<sub>4</sub>/Bi<sub>4</sub>O, g-C<sub>3</sub>N<sub>4</sub>/Bi<sub>4</sub>O<sub>5</sub>I<sub>2</sub>, carbon dots/g-C<sub>3</sub>N<sub>4</sub> and WO<sub>3</sub>/g-C<sub>3</sub>N<sub>4</sub> [138–140].

## Hydrogen generation

Semiconductor photocatalyst g-C<sub>3</sub>N<sub>4</sub> has the proper band edge potential for water splitting applications (Eqs. 14, 15)

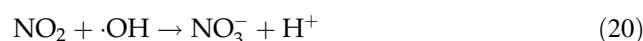
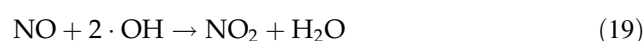


Also, g-C<sub>3</sub>N<sub>4</sub> can be further modified in different routes for improving its H<sub>2</sub> generation ability. So far, g-C<sub>3</sub>N<sub>4</sub> nanosheets, mesoporous g-C<sub>3</sub>N<sub>4</sub> nanomesh, g-C<sub>3</sub>N<sub>4</sub> nanorods, and g-C<sub>3</sub>N<sub>4</sub> quantum dots have shown enhanced H<sub>2</sub> production activity than that of bulk g-C<sub>3</sub>N<sub>4</sub>. Coupling of g-C<sub>3</sub>N<sub>4</sub> with metal/non-metal nanoparticles and other semiconductor materials could extend their spectral range. Generally, F, C, S, I, and P-doped g-C<sub>3</sub>N<sub>4</sub> are used for H<sub>2</sub> generation, showing enhanced production of H<sub>2</sub>. Rh, Pt, Ag, Au, Zn, and Sn-doped g-C<sub>3</sub>N<sub>4</sub> nanocomposites promote H<sub>2</sub> productivity. For instance, FeP/g-C<sub>3</sub>N<sub>4</sub> nanocomposites prepared by Zeng et al. (2018) exhibited outstanding H<sub>2</sub> production activity under visible light exposure. When the loading content of FeP was 2.19%, the catalyst exhibited the maximum production yield of H<sub>2</sub> (177.9  $\mu\text{mol g}^{-1} \text{ h}^{-1}$ ) with an apparent quantum yield (AQY) value of 1.57% at 420 nm. Excellent hydrogen evolution was attributed to active sites formation and heterojunctions [141]. In another research on photocatalytic generation of H<sub>2</sub>, the composite structure comprising of 1D/2D Co<sub>2</sub>P/g-C<sub>3</sub>N<sub>4</sub> heterostructure by solution phase approach

showed improved photocatalytic hydrogen generation without the support of noble metals as cocatalysts. Maximum H<sub>2</sub> production (53.3  $\mu\text{mol h}^{-1} \text{ g}^{-1}$ ) was achieved at an optimum Co<sub>2</sub>P nanorods loading of 3 wt% [142]. In addition, porous g-C<sub>3</sub>N<sub>4</sub> nanosheets modified with flower-like and network-like MoSe<sub>2</sub> nanostructures generate H<sub>2</sub> amount of 114.5  $\mu\text{mol h}^{-1} \text{ g}^{-1}$  and 136.8  $\mu\text{mol h}^{-1} \text{ g}^{-1}$ , respectively. The optimal loading of MoSe<sub>2</sub> nanostructures is 5 wt%, giving maximum H<sub>2</sub> evolution rates of 114.5  $\mu\text{mol h}^{-1} \text{ g}^{-1}$  and 136.8  $\mu\text{mol h}^{-1} \text{ g}^{-1}$ , respectively. In addition, more amount of H<sub>2</sub> generation was achieved over network-like MoSe<sub>2</sub> nanostructures decorated than flower-like MoSe<sub>2</sub>, ascribed to the effective charge migration and separation based on synergistic effects arising from the unique sheet-on-sheet heterointerface in N-CN [143]. Similarly, TiO<sub>2</sub>/g-C<sub>3</sub>N<sub>4</sub>, InO<sub>3</sub>/g-C<sub>3</sub>N<sub>4</sub>, MoS<sub>2</sub>/g-C<sub>3</sub>N<sub>4</sub>, CeO<sub>2</sub>/g-C<sub>3</sub>N<sub>4</sub>, NiO/g-C<sub>3</sub>N<sub>4</sub>, CdS/g-C<sub>3</sub>N<sub>4</sub>, Al<sub>2</sub>O<sub>3</sub>/g-C<sub>3</sub>N<sub>4</sub>, and Cu(OH)<sub>2</sub>/g-C<sub>3</sub>N<sub>4</sub> heterojunctions have been widely studied as photocatalyst for H<sub>2</sub> generation reaction [144–149].

## NO and N<sub>2</sub> fixation

Photocatalytic technology is a promising route in air purification technology, particularly because it does not associate with increased secondary pollution. Self-structure-modified graphene-like g-C<sub>3</sub>N<sub>4</sub> nanosheets enlarge the band gap, inducing strong oxidation of NO to NO<sub>2</sub><sup>-</sup> or NO<sub>3</sub> under visible light exposure [19].



Co-functionalization O/La, O/Ba, and SrO on the surface of amorphous carbon nitride promotes the formation of localized electrons, thus boosting photocatalytic NO removal efficiency [68, 69, 150]. Cui et al. [69] proposed the conversion pathway for NO adsorption and photocatalytic NO oxidation processes on SrO-clusters@amorphous carbon nitride composites [68, 69, 150]. Nearly 100% improved NO purification efficiency was achieved over O, K-functionalized g-C<sub>3</sub>N<sub>4</sub> with IVDWHs [70]. Li et al. [151]

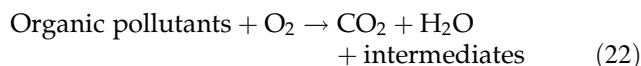
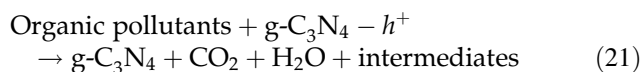
demonstrated that photocatalytic efficiency and selectivity of Ca intercalated  $g\text{-C}_3\text{N}_4$  for NO removal can be considerably enhanced because of the functionality of the localized excess electrons around Ca. In another case, incorporation of Sr caused uneven electron distribution on the surface of  $g\text{-C}_3\text{N}_4$ , accelerating light absorption ability, separation, and transfer of photogenerated charge carriers. As a result,  $\text{NO}_x$  is efficiently oxidized by active species and transformed into target products of  $\text{NO}_2^-$  and  $\text{NO}_3^-$  rather than other toxic by-products [152]. Coexisting of K and Cl ions in the interlayer of  $g\text{-C}_3\text{N}_4$  not only suppresses charge transfer barrier but also acts as the dual channel for electrons and holes transfer to extend their lifetime, thereby improving  $\text{NO}_x$  removal efficiency under visible light exposure as compared with pristine  $g\text{-C}_3\text{N}_4$  and K- $g\text{-C}_3\text{N}_4$ . Moreover, CN-KCl (3%) showed best photocatalytic activity with  $\text{NO}_x$  removal ratio of 38.4%, even more than K doped  $g\text{-C}_3\text{N}_4$  (31.4%) [71]. Moreover, Chen et al. [153] prepared  $\text{MnO}_x/g\text{-C}_3\text{N}_4$  catalyst that were relatively stable and had synergistic photothermal catalytic activity toward NO purification under UV–visible light irradiation. These researchers also proposed the corresponding conversion pathway and mechanism of NO oxidation at 60 °C [153].

NVs (nitrogen vacancy) endow  $g\text{-C}_3\text{N}_4$  with photocatalytic  $\text{N}_2$  fixation ability for three reasons. NVs exhibits the same size and shape of as the nitrogen atom, as a result it selectively adsorb and activate  $\text{N}_2$ . Second, NVs effectively progress the charge separation efficiency of photogenerated carriers and generate more photoelectrons. Third, NVs promote photogenerated electron transfer from  $g\text{-C}_3\text{N}_4$  to adsorbed  $\text{N}_2$ . All three reasons make photocatalytic  $\text{N}_2$  fixation on the surface of V- $g\text{-C}_3\text{N}_4$  easier. Chen et al. [154] systematically investigated single transition metal atoms decorated on the  $g\text{-C}_3\text{N}_4$  with nitrogen vacancies ( $\text{TM@NVs-g-C}_3\text{N}_4$ ), performing as electrocatalysts for conversion of  $\text{N}_2$  into  $\text{NH}_3$ .

### Organic pollutant degradation

Due to the band position,  $g\text{-C}_3\text{N}_4$  is among the best known photocatalysts for the remediation of pollutants present in aqueous solutions. Generally,  $\text{O}_2^-$ ,  $\cdot\text{OH}$ , and  $h^+$  play a substantial role in degrading

different organic pollutants into  $\text{CO}_2$ ,  $\text{H}_2\text{O}$ , and fractions of organic acids as explained in Eqs. (21, 22).



Initially, the organic pollutant is transferred into the interphase of  $g\text{-C}_3\text{N}_4$  and aqueous solution. Then, the adsorbed particles get oxidized or decomposed by ROS species. After that, degradation products (intermediates) are desorbed from  $g\text{-C}_3\text{N}_4$  surface to its interface. Lastly, reaction products get released to the bulk solution. The structure and preparation methodologies of  $g\text{-C}_3\text{N}_4$  influence the degradation efficiency of organic pollutants. As compared with the bulk  $g\text{-C}_3\text{N}_4$ , exfoliated  $g\text{-C}_3\text{N}_4$  nanosheets display improved methylene blue degradation efficiency. Several studies have been available for surface modification of  $g\text{-C}_3\text{N}_4$  by depositing metal nanoparticles (e.g., Ag, Au, Pt, Pd, and Ni) on its surface to degrade organic contaminants from wastewater under visible light irradiation. Correspondingly, hybrid nanostructures built by depositing  $g\text{-C}_3\text{N}_4$  with other semiconductor materials ( $\text{TiO}_2$ , ZnO, AgX (X = Br, Cl, and I),  $\text{Ag}_2\text{O}$ ,  $\text{Ag}_2\text{CO}_3$ ,  $\text{Ag}_3\text{VO}_4$ ,  $\text{Fe}_3\text{O}_4$ , and  $\text{Bi}_2\text{MoO}_6$ ,  $\text{CaIn}_2\text{S}_4$ , C-dots,  $\text{V}_2\text{O}_5$ , CdS, BiOBr, etc.) also revealed better visible light photodegradation for pollutants than pure  $g\text{-C}_3\text{N}_4$ .

### Sensing and bioimaging application

$g\text{-C}_3\text{N}_4$  nanosheet offers more surface area-to-volume ratio and have strong response for detection of various metal ions like  $\text{Cu}^{2+}$ ,  $\text{Fe}^{3+}$ ,  $\text{Hg}^{2+}$ , and  $\text{Cr}^{2+}$  [32]. Also, Fe/ $g\text{-C}_3\text{N}_4$ ,  $g\text{-C}_3\text{N}_4$  nanosheet/ $\text{MnO}_2$  and proton functionalized ultrathin  $g\text{-C}_3\text{N}_4$  nanosheets can detect glucose, glutathione (GSH), and heparin molecules, respectively [155]. Additionally,  $g\text{-C}_3\text{N}_4$  can also be used for temperature sensing as reported by Debanjan et al. [21]. They found that the photoluminescence PL intensity is decreased as the temperature increased. Owing to its non-toxicity, metal-free nature, and high stability,  $g\text{-C}_3\text{N}_4$  nanosheets and nanodots are promising candidates for cell imaging. For example,  $g\text{-C}_3\text{N}_4$  QDs have been utilized as biomarkers for the labeling of the cell membranes [156].

## Conclusion

Photocatalytic disinfection process offers good prospects for biomedical, water treatment, and food applications. In comparison with metal oxides, g-C<sub>3</sub>N<sub>4</sub> can offer a safe and reliable disinfection technology. Visible light-driven g-C<sub>3</sub>N<sub>4</sub>-based materials are a promising and innovative approach for antimicrobial applications. It is clear from several findings that physical and chemical properties of g-C<sub>3</sub>N<sub>4</sub>-based composites can offer acceptable levels of microbial inactivation. The fundamental properties of g-C<sub>3</sub>N<sub>4</sub> and their action against microbial species inactivation have been discussed. Inactivation of the wide range of microorganisms is attributed to the formation of ROS species on the surface of g-C<sub>3</sub>N<sub>4</sub> during the photocatalysis process. Various kinds of g-C<sub>3</sub>N<sub>4</sub> modification techniques (cationic and anionic doping, coupling with another semiconductor material, and surface sensitization) are effective approaches. Furthermore, the photocatalytic disinfection activity of protozoa is not yet well known. Currently, most of the g-C<sub>3</sub>N<sub>4</sub>-based photodisinfection applications are developed and tested in under laboratory conditions. Issues on efficiency due to faster recombination of photogenerated electron–hole pairs need to be addressed. However, it is necessary to investigate the experimental and theoretical aspect of tri-s-triazine-based g-C<sub>3</sub>N<sub>4</sub> for photocatalysis process so as to help to predict reaction pathways as well as band structure changes of g-C<sub>3</sub>N<sub>4</sub> after being hybridizing with certain materials. In addition to the charge separation mechanism, thermodynamics and kinetics study of photocatalytic reaction thorough investigation.

## Acknowledgements

This work did not receive any specific grant from funding agencies in the public, commercial, or not-for-profit sectors.

## Compliance with ethical standards

**Conflict of interest** The authors declare that they have no conflict of interest.

## References

- [1] Kramer A, Schwebke I, Kampf G (2006) How long do nosocomial pathogens persist on inanimate surfaces? A systematic review. *BMC Infect Dis* 6:1–8
- [2] Paul NC, Sullivan TS, Shah DH (2017) Differences in antimicrobial activity of chlorine against twelve most prevalent poultry-associated *Salmonella* serotypes. *Food Microbiol* 64:202–209
- [3] Feliziani E, Lichter A, Smilanick JL, Ippolito A (2016) Disinfecting agents for controlling fruit and vegetable diseases after harvest. *Postharvest Biol Technol* 122:53–69
- [4] Memarzadeh F, Olmsted RN, Bartley JM (2010) Applications of ultraviolet germicidal irradiation disinfection in health care facilities: effective adjunct, but not stand-alone technology. *Am J Infect Control* 38:13–24
- [5] Guo M, Huang J, Hu H et al (2012) UV inactivation and characteristics after photoreactivation of *Escherichia coli* with plasmid: health safety concern about UV disinfection. *Water Res* 46:4031–4036
- [6] Visnapuu M, Rosenberg M, Truska E et al (2018) UVA-induced antimicrobial activity of ZnO/Ag nanocomposite covered surfaces. *Colloids Surf B Biointerfaces* 169:222–232
- [7] Wang Y, Wu Y, Yang H et al (2016) Doping TiO<sub>2</sub> with boron or/and cerium elements: effects on photocatalytic antimicrobial activity. *Vacuum* 131:58–64
- [8] Wu MJ, Bak T, Moffitt MC et al (2014) Photocatalysis of titanium dioxide for water disinfection: challenges and future perspectives. *Int J Photochem* 2014:1–9
- [9] Dimapilis EAS, Hsu CS, Mendoza RMO, Lu MC (2018) Zinc oxide nanoparticles for water disinfection. *Sustain Environ Res* 28:47–56
- [10] Gondal MA, Khalil A (2008) Rapid disinfection of E-Coliform contaminated water using WO<sub>3</sub> semiconductor catalyst by laser-induced photo-catalytic process. *J Environ Sci Health Part A Toxic Hazard Subst Environ Eng* 43:488–494
- [11] Chen M, Zhang F, Oh W (2011) Fabrication and performances of MWCNT/TiO<sub>2</sub> composites derived from MWCNTs and titanium (IV) alkoxide precursors. *Bull Mater Sci* 34:835–841
- [12] Fernández-Ibáñez P, Polo-López MI, Malato S et al (2015) Solar photocatalytic disinfection of water using titanium dioxide graphene composites. *Chem Eng J* 261:36–44
- [13] Wang B, Jiang Z, Yu JC (2019) Treated rape pollen: a metal-free visible-light-driven photocatalyst from nature for efficient water disinfection. *J Mater Chem A* 7:9335–9344
- [14] Ren Y, Zeng D, Ong W (2019) Interfacial engineering of graphitic carbon nitride (g-C<sub>3</sub>N<sub>4</sub>)-based metal sulfide



- heterojunction photocatalysts for energy conversion: a review. *Chin J Catal* 40:289–319
- [15] Wu WS, Wu FG (2018) Two-dimensional materials for antimicrobial applications: graphene materials and beyond. *Chem Asian J* 13:3378–3410
- [16] Wang X, Maeda K, Thomas A et al (2008) A metal-free polymeric photocatalyst for hydrogen production from water under visible light. *Nat Mater* 8:76–80
- [17] Dong G, Zhang Y, Pan Q, Qiu J (2014) A fantastic graphitic carbon nitride (g-C<sub>3</sub>N<sub>4</sub>) material: electronic structure, photocatalytic and photoelectronic properties. *J Photochem Photobiol C Photochem Rev* 20:33–50
- [18] Naseri A, Samadi M, Pourjavadi A et al (2017) Graphitic carbon nitride (g-C<sub>3</sub>N<sub>4</sub>)-based photocatalysts for solar hydrogen generation: recent advances and future development directions. *J Mater Chem A* 5:23406–23433
- [19] Li Y, Sun Y, Ho W et al (2018) Highly enhanced visible-light photocatalytic NO<sub>x</sub> purification and conversion pathway on self-structurally modified g-C<sub>3</sub>N<sub>4</sub> nanosheets. *Sci Bull* 63:609–620
- [20] Yu K, Hu X, Yao K et al (2017) Preparation of an ultrathin 2D/2D rGO/g-C<sub>3</sub>N<sub>4</sub> nanocomposite with enhanced visible-light-driven photocatalytic performance. *RSC Adv* 7:36793–36799
- [21] Das D, Shinde SL, Nanda KK (2015) Temperature-dependent photoluminescence of g-C<sub>3</sub>N<sub>4</sub>: implication for temperature sensing. *ACS Appl Mater Interfaces* 8:2181–2186
- [22] Zhang C, Li Y, Shuai D et al (2018) Graphitic carbon nitride (g-C<sub>3</sub>N<sub>4</sub>)-based photocatalysts for water disinfection and microbial control: a review. *Chemosphere* 214:462–479
- [23] Zimbone M, Buccheri MA, Cacciato G et al (2015) Photocatalytic and antibacterial activity of TiO<sub>2</sub> nanoparticles obtained by laser ablation in water. *Appl Catal B Environ* 165:487–494
- [24] Ehtisham Khan M, Hiep Han T, Mansoob Khan M et al (2018) Environmentally sustainable fabrication of Ag@g-C<sub>3</sub>N<sub>4</sub> nanostructures and their multifunctional efficacy as antibacterial agents and photocatalysts. *ACS Appl Nano Mater* 1(6):2912–2922
- [25] Tao Y, Ni Q, Wei M et al (2015) Metal-free activation of peroxydisulfate by g-C<sub>3</sub>N<sub>4</sub> under visible light irradiation for the degradation of organic dyes. *RSC Adv* 5:44128–44136
- [26] Shanmugam V, Lakshmi A, Jayavel S, Sundar K (2018) Construction of high efficient g-C<sub>3</sub>N<sub>4</sub> nanosheets combined with Bi<sub>2</sub>MoO<sub>6</sub>-Ag photocatalysts for visible-light-driven photocatalytic activity and inactivation of bacteria. *Arab J Chem*. <https://doi.org/10.1016/j.arabjc.2018.05.009>
- [27] Thurston JH, Hunter NM, Wayment LJ, Cornell KA (2017) Urea-derived graphitic carbon nitride (u-g-C<sub>3</sub>N<sub>4</sub>) films with highly enhanced antimicrobial and sporicidal activity. *J Colloid Interface Sci* 505:910–918
- [28] Thurston JH, Hunter NM, Cornell KA (2016) Preparation and characterization of photoactive antimicrobial graphitic carbon nitride (g-C<sub>3</sub>N<sub>4</sub>) films. *RSC Adv* 6:42240–42248
- [29] Fu J, Yu J, Jiang C, Cheng B (2018) g-C<sub>3</sub>N<sub>4</sub>-based heterostructured photocatalysts. *Adv Energy Mater* 8:1–31
- [30] Liebig J (1834) Über einige Stickstoff-Verbindungen. *Annalen der Pharmacie. Eur J Organ Chem* 10:1–47
- [31] Zhou Z, Zhang Y, Shen Y et al (2018) Molecular engineering of polymeric carbon nitride: advancing applications from photocatalysis to biosensing and more. *Chem Soc Rev* 47:2298–2321
- [32] Wang A, Wang C, Fu L et al (2017) Recent advances of graphitic carbon nitride-based structures and applications in catalyst, sensing, imaging, and LEDs. *Nano-Micro Lett* 9:47
- [33] Zhu J, Xiao P, Li H, Carabineiro SC (2014) Graphitic carbon nitride: synthesis, properties, and applications in catalysis. *ACS Appl Mater Interfaces* 6:16449–16465
- [34] Thomas A, Fischer A, Goettmann F et al (2008) Graphitic carbon nitride materials: variation of structure and morphology and their use as metal-free catalysts. *J Mater Chem* 18:4893
- [35] Praus P, Svoboda L, Ritz M et al (2017) Graphitic carbon nitride: synthesis, characterization and photocatalytic decomposition of nitrous oxide. *Mater Chem Phys* 193:438–446
- [36] Dong R, Tian B, Zeng C et al (2012) Ecofriendly synthesis and photocatalytic activity of uniform cubic Ag@AgCl plasmonic photocatalyst. *J Phys Chem C* 4:213–220
- [37] Zheng Y, Liu J, Liang JJ et al (2012) Graphitic carbon nitride materials: controllable synthesis and applications in fuel cells and photocatalysis. *Energy Environ Sci* 5:6717–6731
- [38] Fanchini G, Tagliaferro A, Conway NMJ, Godet C (2002) Role of lone-pair interactions and local disorder in determining the interdependency of optical constants of a -CN:H thin films. *Phys Rev B* 66:195415
- [39] Lyth SM, Nabae Y, Moriya S et al (2009) Carbon nitride as a nonprecious catalyst for electrochemical oxygen reduction. *J Phys Chem C* 113:20148–20151
- [40] Dong G, Zhang L (2012) Porous structure dependent photoreactivity of graphitic carbon nitride under visible light. *J Mater Chem* 22:1160–1166
- [41] Zhou J, Chen W, Sun C et al (2017) Oxidative polyoxometalates modified graphitic carbon nitride for visible-

- light CO<sub>2</sub> reduction. *ACS Appl Mater Interfaces* 9:11689–11695
- [42] Yu J, Wang K, Xiao W, Cheng B (2014) Photocatalytic reduction of CO<sub>2</sub> into hydrocarbon solar fuels over g-C<sub>3</sub>N<sub>4</sub>-Pt nanocomposite photocatalysts. *Phys Chem Chem Phys* 16:11492
- [43] Mao J, Peng T, Zhang X et al (2013) Effect of graphitic carbon nitride microstructures on the activity and selectivity of photocatalytic CO<sub>2</sub> reduction under visible light. *Catal Sci Technol* 3:1253
- [44] Xia J, Di J, Yin S et al (2014) Solvothermal synthesis and enhanced visible-light photocatalytic decontamination of bisphenol A (BPA) by g-C<sub>3</sub>N<sub>4</sub>/BiOBr heterojunctions. *Mater Sci Semicond Process* 24:96–103
- [45] Wang Y, Zhao S, Zhang Y et al (2018) Facile synthesis of self-assembled g-C<sub>3</sub>N<sub>4</sub> with abundant nitrogen defects for photocatalytic hydrogen evolution. *ACS Sustain Chem Eng* 6:10200–10210
- [46] Hu C, Chu Y, Wang M, Wu X (2017) Rapid synthesis of g-C<sub>3</sub>N<sub>4</sub> spheres using microwave-assisted solvothermal method for enhanced photocatalytic activity. *J Photochem Photobiol A Chem* 348:8–17
- [47] Papailias I, Giannakopoulou T, Todorova N et al (2015) Effect of processing temperature on structure and photocatalytic properties of g-C<sub>3</sub>N<sub>4</sub>. *Appl Surf Sci* 358:278–286
- [48] Guo Q, Xie Y, Wang X et al (2003) Characterization of well-crystallized graphitic carbon nitride nanocrystallites via a benzene-thermal route at low temperatures. *Chem Phys Lett* 380:84–87
- [49] Guo Q, Yang Q, Zhu L et al (2004) A facile one-pot solvothermal route to tubular forms of luminescent. *Solid State Commun* 132:369–374
- [50] Dai H, Gao X, Liu E et al (2013) Synthesis and characterization of graphitic carbon nitride sub-microspheres using microwave method under mild condition. *Diam Relat Mater* 38:109–117
- [51] Hu C, Chu Y, Wang M, Wu X (2017) Rapid synthesis of g-C<sub>3</sub>N<sub>4</sub> spheres using microwave-assisted solvothermal method for enhanced photocatalytic activity. *J Photochem Photobiol A Chem* 348:8–17
- [52] Wang J, Miller DR, Gillan EG (2002) Photoluminescent carbon nitride films grown by vapor transport of carbon nitride powders. *Chem Commun* 19:2258–2259
- [53] Kang S, Huang W, Zhang L et al (2018) Moderate bacterial etching allows scalable and clean delamination of g-C<sub>3</sub>N<sub>4</sub> with enriched unpaired electrons for highly improved photocatalytic water disinfection. *ACS Appl Mater Interfaces* 10:13796–13804
- [54] Zhou S, Liu Y, Li J et al (2014) Facile in situ synthesis of graphitic carbon nitride (g-C<sub>3</sub>N<sub>4</sub>)-N-TiO<sub>2</sub> heterojunction as an efficient photocatalyst for the selective photoreduction of CO<sub>2</sub> to CO. *Appl Catal B Environ* 158–159:20–29
- [55] Ye L, Wu D, Chu KH et al (2016) Phosphorylation of g-C<sub>3</sub>N<sub>4</sub> for enhanced photocatalytic CO<sub>2</sub> reduction. *Chem Eng J* 304:376–383
- [56] Dong F, Zhao Z, Xiong T et al (2013) In situ construction of g-C<sub>3</sub>N<sub>4</sub>/g-C<sub>3</sub>N<sub>4</sub> metal-free heterojunction for enhanced visible-light photocatalysis. *ACS Appl Mater Interfaces* 5:11392–11401
- [57] Jing L, Xu Y, Chen Z, He M (2018) Different morphologies SnS<sub>2</sub> supported on 2D g-C<sub>3</sub>N<sub>4</sub> for excellent and stable visible light photocatalytic hydrogen generation. *ACS Sustain Chem Eng* 6:5132–5141
- [58] Teng Z, Yang N, Lv H et al (2018) Edge-functionalized g-C<sub>3</sub>N<sub>4</sub> nanosheets as a highly efficient metal-free photocatalyst for safe drinking water. *Chem* 5:1–17
- [59] Liang S, Zhang D, Pu X et al (2019) Separation and purification technology a novel Ag<sub>2</sub>O/g-C<sub>3</sub>N<sub>4</sub> p-n heterojunction photocatalysts with enhanced visible and near-infrared light activity. *Sep Purif Technol* 210:786–797
- [60] Wang XJ, Tian X, Sun YJ, Zhu JY, Li FT, Mu HY, Zhao J (2018) Enhanced Schottky effect of a 2D–2D CoP/g-C<sub>3</sub>N<sub>4</sub> interface for boosting photocatalytic H<sub>2</sub> evolution. *Nanoscale* 10(26):12315–12321
- [61] Xia K, Chen Z, Yi J et al (2018) Highly efficient visible-light-driven schottky catalyst MoN/2D g-C<sub>3</sub>N<sub>4</sub> for hydrogen production and organic pollutants degradation. *Ind Eng Chem Res* 57:8863–8870
- [62] Shen Y, Zhu Z, Wang X et al (2018) Synthesis of Z-scheme g-C<sub>3</sub>N<sub>4</sub>/Ag/Ag<sub>3</sub>PO<sub>4</sub> composite for enhanced photocatalytic degradation of phenol and selective oxidation of gaseous isopropanol. *Mater Res Bull* 107:407–415
- [63] Kroke E, Schwarz M, Horath-bordon E et al (2002) Tri-s-triazine derivatives. Part I. From trichloro-tri-s-triazine to graphitic C<sub>3</sub>N<sub>4</sub> structures y. *New J Chem* 26:508–512
- [64] Wen J, Xie J, Chen X, Li X (2017) A review on g-C<sub>3</sub>N<sub>4</sub>-based photocatalysts. *Appl Surf Sci* 391:72–123
- [65] Cao S, Low J, Yu J, Jaroniec M (2015) Polymeric photocatalysts based on graphitic carbon nitride. *Adv Mater* 27:2150–2176
- [66] Wang Y, Wang X, Antonietti M (2012) Polymeric graphitic carbon nitride as a heterogeneous organocatalyst: from photochemistry to multipurpose catalysis to sustainable chemistry. *Angew Chem Int Ed* 51:68–89
- [67] Li S, Wang Z, Wang X et al (2017) Orientation controlled preparation of nanoporous carbon nitride fibers and related composite for gas sensing under ambient conditions. *Nano Res* 10:1710–1719
- [68] Chen P, Wang H, Liu H et al (2018) Directional electron delivery and enhanced reactants activation enable efficient

- photocatalytic air purification on amorphous carbon nitride Co-functionalized with O/La. *Appl Catal B Environ* 242:19–30
- [69] Cui AW, Li J, Sun Y, Wang H (2018) Enhancing ROS generation and suppressing toxic intermediate production in photocatalytic NO oxidation on O/Ba co-functionalized amorphous carbon nitride. *Appl Catal B Environ* 237:938–946
- [70] Li J, Zhang Z, Cui W, Wang H, Cen W, Johnson G, Jiang G, Zhang S, Dong F (2018) The spatially oriented charge flow and photocatalysis mechanism on internal van der Waals heterostructures enhanced g-C<sub>3</sub>N<sub>4</sub>. *ACS Catal* 8:8376–8385
- [71] Xiong T, Wang H, Zhou Y, Sun Y, Cen W, Huang H, Zhang Y, Dong F (2018) KCl-mediated dual electronic channels in layered g-C<sub>3</sub>N<sub>4</sub> for enhanced visible light photocatalytic NO removal. *Nanoscale* 10:8066–8074
- [72] Cui J, Liang S, Wang X, Zhang J (2015) First principle modeling of oxygen-doped monolayer graphitic carbon nitride. *Mater Chem Phys* 161:194–200
- [73] Wang J, Guan Z, Huang J, Li Q, Yang J (2014) Enhanced photocatalytic mechanism for the hybrid g-C<sub>3</sub>N<sub>4</sub>/MoS<sub>2</sub> nanocomposite. *J Mater Chem A* 2:7960–7966
- [74] Ji Y, Dong H, Lin H, Zhang L, Hou T, Li Y (2016) Hep-tazine-based graphitic carbon nitride as an effective hydrogen purification membrane. *RSC Adv* 6:52377–52383
- [75] Wirth J, Neumann R, Antonietti M, Saalfrank P (2014) Adsorption and photocatalytic splitting of water on graphitic carbon nitride: a combined first principles and semiempirical study. *PhysChemChemPhys* 16:15917–15926
- [76] Hua E, Liu G, Zhang G, Xu X (2018) In situ fabrication of two-dimensional g-C<sub>3</sub>N<sub>4</sub>/Ba<sub>5</sub>Ta<sub>4</sub>O<sub>15</sub> nanosheet heterostructures with efficient charge separations and photocatalytic hydrogen evolution under visible light illumination. *Dalt Trans* 47:4360–4367
- [77] Adekoya DO, Tahir M, Aishah N, Amin S (2017) g-C<sub>3</sub>N<sub>4</sub>/(Cu/TiO<sub>2</sub>) nanocomposite for enhanced photoreduction of CO<sub>2</sub> to CH<sub>3</sub> OH and HCOOH under UV/visible light. *J CO<sub>2</sub> Util* 18:261–274
- [78] Huang J, Ho W, Wang X (2014) Metal-free disinfection effects induced by graphitic carbon nitride polymers under visible light illumination. *Chem Commun* 50:4338–4340
- [79] Xu J, Wang Z, Zhu Y (2017) Enhanced visible-light-driven photocatalytic disinfection performance and organic pollutant degradation activity of porous g-C<sub>3</sub>N<sub>4</sub> nanosheets. *ACS Appl Mater Interfaces* 9:27727–27735
- [80] Kang S, Huang W, Zhang L et al (2018) Moderate bacterial etching allows scalable and clean delamination of g-C<sub>3</sub>N<sub>4</sub> with enriched unpaired electrons for highly improved photocatalytic water disinfection. *Appl Mater Interfaces* 10:13796–13804
- [81] Zhao H, Yu H, Quan X et al (2014) Fabrication of atomic single layer graphitic-C<sub>3</sub>N<sub>4</sub> and its high performance of photocatalytic disinfection under visible light irradiation. *Appl Catal B Environ* 152–153:46–50
- [82] Li Y, Zhang C, Shuai D et al (2016) Visible-light-driven photocatalytic inactivation of MS<sub>2</sub> by metal-free g-C<sub>3</sub>N<sub>4</sub>: virucidal performance and mechanism. *Water Res* 106:249–258
- [83] Zhang C, Li Y, Zhang W et al (2018) Metal-free virucidal effects induced by g-C<sub>3</sub>N<sub>4</sub> under visible light irradiation: statistical analysis and parameter optimization. *Chemosphere* 195:551–558
- [84] Patra KK, Gopinath CS (2016) Bimetallic and plasmonic Ag–Au on TiO<sub>2</sub> for solar water splitting: an active nanocomposite for entire visible-light-region absorption. *ChemCatChem* 8:1–9
- [85] Zhang Q, Gangadharan DT, Liu Y et al (2016) Recent advancements in plasmon-enhanced visible light-driven water splitting. *J Materiomics* 3:33–34
- [86] Li S, Zhang J, Kibria MG, Mi Z, Chaker M, Ma D, Nechache R, Rosei F (2013) Remarkably enhanced photocatalytic activity of laser ablated Au nanoparticle decorated BiFeO<sub>3</sub> nanowires under visible-light. *Chem Commun* 49:5856–5858
- [87] Xue J, Ma S, Zhou Y et al (2015) Facile photochemical synthesis of Au/Pt/g-C<sub>3</sub>N<sub>4</sub> with plasmon-enhanced photocatalytic activity for antibiotic degradation. *ACS Appl Mater Interfaces* 7:9630–9637
- [88] Qin J, Huo J et al (2015) Improving photocatalytic hydrogen production of Ag/g-C<sub>3</sub>N<sub>4</sub> nanocomposites by dye-sensitization under visible light irradiation. *Nanoscale* 8:2249–2259
- [89] Bing W, Chen Z, Sun H et al (2015) Visible-light-driven enhanced antibacterial and bio film elimination activity of graphitic carbon nitride by embedded Ag nanoparticles. *Nano Res* 8:1648–1658
- [90] Ma S, Zhan S, Jia Y et al (2016) Enhanced disinfection application of Ag-modified g-C<sub>3</sub>N<sub>4</sub> composite under visible light. *Appl Catal B Environ* 186:77–87
- [91] Xu J, Gao Q, Bai X et al (2019) Enhanced visible-light-induced photocatalytic degradation and disinfection activities of oxidized porous g-C<sub>3</sub>N<sub>4</sub> by loading Ag nanoparticles. *Catal Today* 332:227–235
- [92] Liu C, Wang L, Xu H et al (2016) one pot green synthesis and the antibacterial activity of g-C<sub>3</sub>N<sub>4</sub>/Ag nanocomposites. *Mater Lett* 164:567–570
- [93] Muñoz-Batista MJ, Fontelles-Carceller O, Ferrer M et al (2016) Disinfection capability of Ag/g-C<sub>3</sub>N<sub>4</sub> composite

- photocatalysts under UV and visible light illumination. *Appl Catal B Environ* 183:86–95
- [94] Wang Z, Dong K, Liu Z et al (2016) Activation of biologically relevant levels of reactive oxygen species by Au/g-C<sub>3</sub>N<sub>4</sub> hybrid nanozyme for bacteria killing and wound disinfection. *Biomaterials* 113:145–157
- [95] Wang W, Li G, An T, Chan DKL, Yu JC, Wong PK (2018) Photocatalytic hydrogen evolution and bacterial inactivation utilizing sonochemical-synthesized g-C<sub>3</sub>N<sub>4</sub>/red phosphorus hybrid nanosheets as a wide-spectral-responsive photocatalyst: the role of type I band alignment. *Appl Catal B Environ* 238:126–135
- [96] Li G, Nie X, Chen J et al (2015) Enhanced visible-light-driven photocatalytic inactivation of *E. coli* using g-C<sub>3</sub>N<sub>4</sub>/TiO<sub>2</sub> hybrid photocatalyst synthesized using a hydrothermal-calcination approach. *Water Res* 86:17–24
- [97] Xu J, Li Y, Zhou X et al (2016) Graphitic C<sub>3</sub>N<sub>4</sub>-sensitized TiO<sub>2</sub> nanotube layers: a visible-light activated efficient metal-free antimicrobial platform. *Chem Eur J* 22:3947–3951
- [98] Zhang Q, Quan X, Wang H et al (2017) Constructing a visible-light-driven photocatalytic membrane by g-C<sub>3</sub>N<sub>4</sub> quantum dots and TiO<sub>2</sub> nanotube array for enhanced water treatment. *Sci Rep* 7:3128
- [99] Liu Y, Zeng X, Hu X et al (2018) Two-dimensional g-C<sub>3</sub>N<sub>4</sub>/TiO<sub>2</sub> nanocomposites as vertical Z-scheme heterojunction for improved photocatalytic water disinfection. *Catal Today*. <https://doi.org/10.1016/j.cattod.2018.11.053>
- [100] Li J, Yin Y, Liu E et al (2017) In situ growing Bi<sub>2</sub>MoO<sub>6</sub> on g-C<sub>3</sub>N<sub>4</sub> nanosheets with enhanced photocatalytic hydrogen evolution and disinfection of bacteria under visible light irradiation. *J Hazard Mater* 321:183–192
- [101] Xia D, Wang W, Yin R et al (2017) Enhanced photocatalytic inactivation of *Escherichia coli* by a novel Z-scheme g-C<sub>3</sub>N<sub>4</sub>/m-Bi<sub>2</sub>O<sub>4</sub> hybrid photocatalyst under visible light: the role of reactive oxygen species. *Appl Catal B Environ* 214:23–33
- [102] Deng J, Liang J, Li M, Tong M (2017) Enhanced visible-light-driven photocatalytic bacteria disinfection by g-C<sub>3</sub>N<sub>4</sub>-AgBr. *Colloids Surf B Biointerfaces* 152:49–57
- [103] Li Y, Li Y, Ma S et al (2017) Efficient water disinfection with Ag<sub>2</sub>WO<sub>4</sub>-doped mesoporous g-C<sub>3</sub>N<sub>4</sub> under visible light. *J Hazard Mater* 338:33–46
- [104] Wang R, Kong X, Zhang W et al (2018) Mechanism insight into rapid photocatalytic disinfection of *Salmonella* based on vanadate QDs-interspersed g-C<sub>3</sub>N<sub>4</sub> heterostructures. *Appl Catal B Environ* 225:228–237
- [105] Wang AW, An T, Li G, Xia D (2017) Earth-abundant Ni<sub>2</sub>P/g-C<sub>3</sub>N<sub>4</sub> lamellar nanohybrids for enhanced photocatalytic hydrogen evolution and bacterial inactivation under visible light irradiation. *Appl Catal B Environ* 217:570–580
- [106] Vidyasagar D, Ghugal SG, Kulkarni A, Shende AG, Umare SS, Sasikala R (2018) Microwave assisted in situ decoration of g-C<sub>3</sub>N<sub>4</sub> surface with CdCO<sub>3</sub> nanoparticles for visible light driven photocatalysis. *New J Chem* 42:6322–6331
- [107] Sundaram IM, Kalimuthu S, Ponniah GP (2017) Highly active ZnO modified g-C<sub>3</sub>N<sub>4</sub> nanocomposite for dye degradation under UV and visible light with enhanced stability and antimicrobial activity. *Compos Commun* 5:64–71
- [108] Ong W (2017) 2D/2D graphitic carbon nitride nanocomposites for photocatalysis: why does face-to-face interface. *Front Mater* 4:1–10
- [109] Sun L, Du T, Hu C et al (2017) Antibacterial activity of graphene oxide/g-C<sub>3</sub>N<sub>4</sub> composite through photocatalytic disinfection under visible light. *ACS Sustain Chem Eng* 5:8693–8701
- [110] Wang W, Yu JC, Xia D et al (2013) Graphene and g-C<sub>3</sub>N<sub>4</sub> nanosheets cowrapped elemental  $\alpha$ -sulfur as a novel metal-free heterojunction photocatalyst for bacterial inactivation under visible-light. *Environ Sci Technol* 47:8724–8732
- [111] Ouyang K, Dai K, Chen H et al (2017) Metal-free inactivation of *E. coli* O157:H7 by fullerene/C<sub>3</sub>N<sub>4</sub> hybrid under visible light irradiation. *Ecotoxicol Environ Saf* 136:40–45
- [112] Zhang C, Li Y, Shuai D et al (2018) Visible-light-driven, water-surface-floating antimicrobials developed from graphitic carbon nitride and expanded perlite for water disinfection. *Chemosphere* 208:84–92
- [113] Adhikari SPAGP, Lee J, Park CH, Kim CS (2016) Synthesis, characterization, organic compound degradation activity and antimicrobial performance of g-C<sub>3</sub>N<sub>4</sub> sheets customized with metal nanoparticle-decorated TiO<sub>2</sub> nanofibers. *RSC Adv* 6:55079–55091
- [114] Joo H, Chan K, Park H, Sang C (2015) One pot synthesis and characterization of Ag-ZnO/g-C<sub>3</sub>N<sub>4</sub> photocatalyst with improved photoactivity and antibacterial properties. *Colloids Surf A* 482:477–484
- [115] Pant B, Park M, Lee JH et al (2017) Novel magnetically separable silver-iron oxide nanoparticles decorated graphitic carbon nitride nano-sheets: a multifunctional photocatalyst via one-step hydrothermal process. *J Colloid Interface Sci* 496:343–352
- [116] Vidyasagar D, Ghugal SG, Kulkarni A et al (2018) Silver/Silver(II) oxide (Ag/AgO) loaded graphitic carbon nitride microspheres: an effective visible light active photocatalyst for degradation of acidic dyes and bacterial inactivation. *Appl Catal B Environ* 221:339–348
- [117] Zhang M, Liu Z, Gao Y, Shu L (2017) Ag modified g-C<sub>3</sub>N<sub>4</sub> composite entrapped PES UF membrane with visible-light-driven photocatalytic antifouling performance. *RSC Adv* 7:42919–42928



- [118] Zeng X, Lan S, Lo IMC (2019) Rapid disinfection of *E. coli* by ternary BiVO<sub>4</sub>/Ag/g-C<sub>3</sub>N<sub>4</sub> composite under visible light: photocatalysis mechanism and performance investigation in authentic sewage. *Environ Sci* 6:610–623
- [119] Lin AT, Son Z, Wu Y et al (2018) Boron- and phenyl-codoped graphitic carbon nitride with greatly enhanced light responsive range for photocatalytic disinfection. *J Hazard Mater* 358:62–68
- [120] Liu B, Han X, Wang Y et al (2018) Synthesis of g-C<sub>3</sub>N<sub>4</sub>/BiOI/BiOBr heterostructures for efficient visible-light-induced photocatalytic and antibacterial activity. *J Mater Sci Mater Electron* 29:14300–14310
- [121] Younis SA, Abd-Elaziz A, Hashem A (2016) Utilization of a pyrrole derivative based antimicrobial functionality impregnated onto CaO/g-C<sub>3</sub>N<sub>4</sub> for dyes adsorption. *RSC Adv* 6:89367–89379
- [122] Zhao H, Chen S, Quan X et al (2016) Environmental integration of microfiltration and visible-light-driven photocatalysis on g-C<sub>3</sub>N<sub>4</sub> nanosheet/reduced graphene oxide membrane for enhanced water treatment. *Appl Catal B Environ* 194:134–140
- [123] Tian Y, Zhou F, Zhan S et al (2018) Mechanisms on the enhanced sterilization performance of fluorocarbon resin composite coatings modified by -C<sub>3</sub>N<sub>4</sub>/Bi<sub>2</sub>MoO<sub>6</sub> under the visible-light. *J Photochem Photobiol A Chem* 350:10–16
- [124] Faraji M, Mohaghegh N, Abedini A (2017) Ternary composite of TiO<sub>2</sub> nanotubes/Ti plates modified by g-C<sub>3</sub>N<sub>4</sub> and SnO<sub>2</sub> with enhanced photocatalytic activity for enhancing antibacterial and photocatalytic activity. *J Photochem Photobiol B Biol* 178:124–132
- [125] Li C, Sun Z, Zhang W et al (2017) Highly efficient g-C<sub>3</sub>N<sub>4</sub>/TiO<sub>2</sub>/kaolinite composite with novel three-dimensional structure and enhanced visible light responding ability towards ciprofloxacin and *S. aureus*. *Appl Catal B Environ* 220:272–282
- [126] Song AJ, Wang X, Ma J (2017) Visible-light-driven in situ inactivation of *Microcystis aeruginosa* with the use of floating g-C<sub>3</sub>N<sub>4</sub> heterojunction photocatalyst: performance, mechanisms and implications. *Appl Catal B Environ* 226:83–92
- [127] Song J, Wang X, Ma J et al (2018) Removal of microcystis aeruginosa and microcystin-LR using a graphitic-C<sub>3</sub>N<sub>4</sub>/TiO<sub>2</sub> floating photocatalyst under visible light irradiation. *Chem Eng J* 348:380–388
- [128] Wang X, Wang X, Zhao J et al (2018) Adsorption-photocatalysis functional expanded graphite C/C composite for in situ photocatalytic inactivation of *Microcystis aeruginosa*. *Chem Eng J* 341:516–525
- [129] Niu P, Yang Y, Yu JC et al (2014) Switching the selectivity of the photoreduction reaction of carbon dioxide by controlling the band structure of a g-C<sub>3</sub>N<sub>4</sub> photocatalyst. *Chem Commun* 50:10837
- [130] Su Q, Sun J, Wang J et al (2014) Urea-derived graphitic carbon nitride as an efficient heterogeneous catalyst for CO<sub>2</sub> conversion into cyclic carbonates. *Catal Sci Technol* 4:1556
- [131] Wang H, Sun Z, Li Q et al (2016) Surprisingly advanced CO<sub>2</sub> photocatalytic conversion over thiourea derived g-C<sub>3</sub>N<sub>4</sub> with water vapor while introducing 200–420 nm UV light. *J CO<sub>2</sub> Util* 14:143–151
- [132] Tahir B, Tahir M, Amin NAS (2017) Photo-induced CO<sub>2</sub> reduction by CH<sub>4</sub>/H<sub>2</sub>O to fuels over Cu-modified g-C<sub>3</sub>N<sub>4</sub> nanorods under simulated solar energy. *Appl Surf Sci* 419:875–885
- [133] Tang JY, Zhou WG, Guo RT, Huang CY, Pan WG (2018) Enhancement of photocatalytic performance in CO<sub>2</sub> reduction over Mg/g-C<sub>3</sub>N<sub>4</sub> catalysts under visible light irradiation. *Catal Commun* 10(107):92–95
- [134] Wang Y, Xu Y, Wang Y et al (2016) Synthesis of Mo-doped graphitic carbon nitride catalysts and their photocatalytic activity in the reduction of CO<sub>2</sub> with H<sub>2</sub>O. *Catal Commun* 74:75–79
- [135] Wang K, Li Q, Liu B et al (2015) Sulfur-doped g-C<sub>3</sub>N<sub>4</sub> with enhanced photocatalytic CO<sub>2</sub>-reduction performance. *Appl Catal B Environ* 176–177:44–52
- [136] Yuan YP, Cao SW, Sen LY et al (2013) Red phosphor/g-C<sub>3</sub>N<sub>4</sub> heterojunction with enhanced photocatalytic activities for solar fuels production. *Appl Catal B Environ* 140–141:164–168
- [137] Kuriki R, Sekizawa K, Ishitani O, Maeda K (2015) Visible-light-driven CO<sub>2</sub> reduction with carbon nitride: enhancing the activity of ruthenium catalysts. *Angew Chem Int Ed* 54:1–5
- [138] Ong W, Putri LK, Tan Y et al (2017) Unravelling charge carrier dynamics in protonated g-C<sub>3</sub>N<sub>4</sub> interfaced with carbon nanodots as co-catalysts toward enhanced photocatalytic CO<sub>2</sub> reduction: a combined experimental and first-principles DFT study. *Nano Res* 10:1673–1696
- [139] Photocatalysis L (2018) g-C<sub>3</sub>N<sub>4</sub>-based nanomaterials for visible light-driven photocatalysis. *Catalyst* 8:74
- [140] Sun Z, Wang H, Wu Z, Wang L (2018) g-C<sub>3</sub>N<sub>4</sub> based composite photocatalysts for photocatalytic CO<sub>2</sub> reduction. *Catal Today* 300:160–172
- [141] Zeng D, Zhou T, Ong W et al (2019) Sub-5 nm ultra-fine FeP nanodots as efficient co-catalysts modified porous g-C<sub>3</sub>N<sub>4</sub> for precious-metal-free photocatalytic hydrogen evolution under visible light. *ACS Appl Mater Interfaces* 11:5651–5660
- [142] Zeng D, Ong W, Chen Y et al (2018) Co2P nanorods as an efficient cocatalyst decorated porous g-C<sub>3</sub>N<sub>4</sub> Nanosheets

- for photocatalytic hydrogen production under visible light irradiation. *Part Part Syst Charact* 35:1700251
- [143] Zeng D, Wu P, Ong W et al (2018) Construction of network-like and flower-like 2H-MoSe<sub>2</sub> nanostructures coupled with porous g-C<sub>3</sub>N<sub>4</sub> for noble-metal-free photocatalytic H<sub>2</sub> evolution under visible light. *Appl Catal B Environ* 233:26–34
- [144] Ye S, Wang R, Wu M, Yuan Y (2015) A review on g-C<sub>3</sub>N<sub>4</sub> for photocatalytic water splitting and CO<sub>2</sub> reduction. *Appl Surf Sci* 358:15–27
- [145] Liu J, Jia Q, Long J et al (2017) Amorphous NiO as cocatalyst for enhanced visible-light-driven hydrogen generation over g-C<sub>3</sub>N<sub>4</sub> photocatalyst. *Appl Catal B Environ* 222:35–43
- [146] Zhou X, Luo Z, Tao P et al (2014) Facile preparation and enhanced photocatalytic H<sub>2</sub>-production activity of Cu(OH)<sub>2</sub> nanospheres modified porous g-C<sub>3</sub>N<sub>4</sub>. *Mater Chem Phys* 143:1462–1468
- [147] Li F, Liu S, Xue Y et al (2015) Structure Modification Function of g-C<sub>3</sub>N<sub>4</sub> for Al<sub>2</sub>O<sub>3</sub> in the in situ hydrothermal process for enhanced photocatalytic activity. *Chem Eur J* 21:10149–10159
- [148] Ji C, Du C, Steinkruger JD et al (2019) In-situ hydrothermal fabrication of CdS/g-C<sub>3</sub>N<sub>4</sub> nanocomposites for enhanced photocatalytic water splitting. *Mater Lett* 240:128–131
- [149] Naseri A, Samadi M, Pourjavadi A et al (2017) Recent advances and future development directions. *J Mater Chem A Mater energy Sustain* 5:23406–23433
- [150] Cui W, Li J, Dong F et al (2017) Highly efficient performance and conversion pathway of photocatalytic NO oxidation on SrO-clusters @ amorphous carbon nitride highly efficient performance and conversion pathway of photocatalytic NO oxidation on SrO-clusters @ amorphous carbon nitride. *Environ Sci Technol* 51:10682–10690
- [151] Li AJ, Dong X, Sun Y (2018) Tailoring the rate-determining step in photocatalysis via localized excess electrons for efficient and safe air cleaning. *Appl Catal B Environ* 239:187–195
- [152] Li J, Dong X, Sun Y, Jiang G, Chu Y, Lee SC, Dong F (2018) Tailoring the rate-determining step in photocatalysis via localized excess electrons for efficient and safe air cleaning. *Appl Catal B Environ* 232:69–76
- [153] Chen P, Dong F, Ran M, Li J (2018) Synergistic photo-thermal catalytic NO purification of MnO<sub>x</sub>/g-C<sub>3</sub>N<sub>4</sub>: enhanced performance and reaction mechanism. *Chin J Catal* 39:619–629
- [154] Chen X, Zhao X, Kong Z, Ong WJ, Li N (2018) Unravelling the electrochemical mechanisms for nitrogen fixation on single transition metal atom embedded in defective graphitic carbon nitride. *J Mater Chem A* 6:21941–21948
- [155] Xu Y, Niu X, Zhang H et al (2015) Switch-on fluorescence sensing of glutathione in food samples based on a g-CNQDs-Hg<sub>2</sub><sup>+</sup> chemosensor. *J Agric Food Chem* 1(63):1747–1755
- [156] Zhan Y, Liu Z, Liu Q, Huang D, Wei Y, Hu Y, Lian X, Hu C (2017) A facile and one-pot synthesis of fluorescent graphitic carbon nitride quantum dots for bio-imaging application. *New J Chem* 41:3930–3938
- [157] Ong W, Tan L, Ng YH et al (2016) Graphitic carbon nitride (g-C<sub>3</sub>N<sub>4</sub>)-based photocatalysts for artificial photosynthesis and environmental remediation: are we a step closer to achieving sustainability? *Chem Rev* 116:7159–7329
- [158] Zhu B, Zhang L, Cheng B, Yu J (2017) First-principle calculation study of tri-s-triazine-based g-C<sub>3</sub>N<sub>4</sub>: a review. *Appl Catal B Environ* 224:983–999
- [159] Xu Y, Gao S (2012) Band gap of C<sub>3</sub>N<sub>4</sub> in the GW approximation. *Int J Hydrogen Energy* 37:11072–11080
- [160] Teter DM, Hemley RJ (2019) Low-compressibility carbon nitrides. *Science* (80-) 271:53–55

**Publisher's Note** Springer Nature remains neutral with regard to jurisdictional claims in published maps and institutional affiliations.